# Studies of X-ray absorption fine structure spectra for complex systems

January 2014

Kei Takahashi

Graduate School of Advanced Integration Science
CHIBA UNIVERSITY

（千葉大学審査学位論文）

# X線吸収微細構造スペクトルによる複雑系に関する研究

## Studies of X-ray absorption fine structure spectra for complex systems

2014年　1月

（平成25年度）

千葉大学大学院融合科学研究科

ナノサイエンス専攻ナノ物性コース

高橋　慧

# Contents

# List of Figures

# List of Tables

# Chapter 1

# Introduction

## 1.1 X-ray absorption fine structure

X-ray absorption fine structure (XAFS) is one kind of the X-ray absorption spectroscopy (XAS). The specific oscillation structure of the absorption spectra was discovered by Kronig in 1923 [4]. Sayers, Stern and Lytle successfully interpreted the oscillation based on the short range order theory in 1971 [5]. They introduced Fourier transformation to EXAFS spectra. The peaks of the Fourier transformed spectra correspond to interatomic distances. XAFS does not require the long range order of the system thus the XAFS spectra has been widely used for structural analysis for vast fields such as inorganic chemistry, biological material, amorphous material, liquid system, etc..

XAFS is associated with the core electron excitation process. When an atom absorb the X-ray e.g. the X-ray energies equals to tightly bound core level electron, the absorption spectra shows the sharp rise at specific X-ray energies called ”edge”. Figure 1.1 shows the X-ray absorption spectrum of iodine as an example. The each edges are called K, $L_I$, $L_{II}$, $L_{III}$, . . ., respectively corresponding to the inner shell from which the photoelectron is excited. The excited energy is specified by each orbital of each atom. Therefore the absorption spectrum shows element and orbital selectivity. L-shell consists of $2s$ and three $2p$ orbitals. The $2p$ orbital is split into $2p_{1/2}$ and $2p_{3/2}$ orbitals due to the relativistic effect. Therefore the absorption edge of L-shell has three edges $L_I$, $L_{II}$ and $L_{III}$ respectively corresponding to $2s$, $2p_{1/2}$ and $2p_{3/2}$.

When an atom absorbs X-rays, a photoelectron is ejected from its core orbital and the atom goes into an excited state. The excited state will decay typically within a few femtoseconds. There are two decay processes of excited atom. One is emitting X-ray fluorescence, in which an electron bound to outer orbital fills core hole by emitting a specific energy X-ray. For instance, an L-shell electron

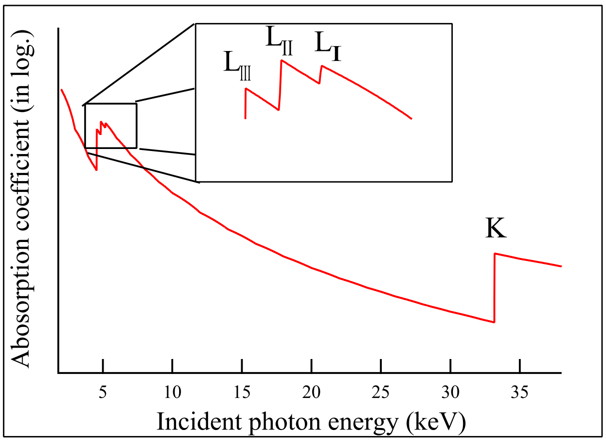

Figure 1.1: X-ray absorption coefficient of iodine as a function of incident photon energy from the table by McMaster et al. [1]. Four X-ray edges are shown.

filling K-shell hole provides the $K_\alpha$ line. The other process of decay is Auger electron emission. In this process, a second electron is emitted into the continuum when an electron bound to outer orbital fills the core hole. Figure 1.2 shows the image of core electron excitation by X-ray and decay of the excitation by emitting X-ray fluorescence or Auger electron. The Auger process is dominant for the light element e.g. the atomic number Z is smaller than 20, but fluorescence process becomes dominant for heavy element [6, 7].

Figure 1.4 shows a simple schematic of a typical experimental setup in transmission mode. The X-ray intensity transmitted though the sample $I$ is given by Beer's Law:

$$I = I_0 e^{-\mu(\omega)t} \tag{1.1}$$

where $I_0$ is the X-ray intensity incident on a sample and $t$ is thickness of the sample. Thus, absorption coefficient $\mu(\omega)$ is described by

$$\mu(\omega) \propto \ln(I_0/I). \tag{1.2}$$

Other methods for measuring absorption are available. For example, absorption can be measured by fluorescence mode where the fluorescence yield is measured instead of the transmitted intensity or Auger electron yield mode.

Figure 1.5 shows typical experimental absorption spectrum of fcc Cu K-edge [8]. The oscillation of the absorption spectra above the edge called ”fine structure” is caused by quantum interference due to the backscattering of the photoelectron

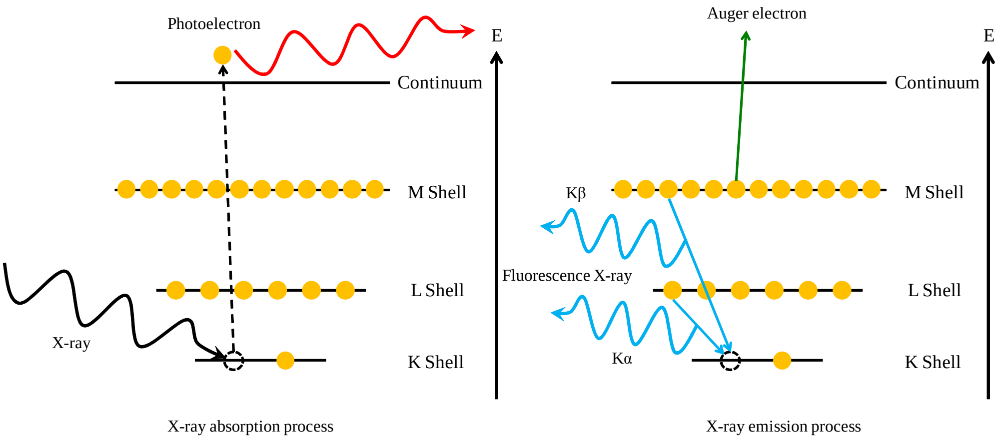

Figure 1.2: Image of core electron excitation by X-ray and de-excitation process with emitting X-ray fluorescence or Auger electron.

which excited by X-ray off the neighboring atom. The fine structure can be observed until about 1000 eV from the absorption edge.

XAFS spectrum is divided into two regions: X-ray absorption near edge structure (XANES) region and extended X-ray absorption fine structure (EXAFS) region. Although there is no exact boundary between the XANES and the EXAFS, the two are commonly divided at about 50 eV above the edge. The analysis of EXAFS has mainly provided radial distances of neighboring atoms and coordination number of X-ray absorbing atom. On the other hand, the analysis of XANES should provide information about the detailed local geometry around the absorbing site.

In the EXAFS region, in which the photoelectron energy is above 50 eV, the scattering from individual atoms tend to be focused in the forward direction. Furthermore, the mean free path of excited electron is reduced because of inelastic losses such as coupling to plasmons or electron-hole pairs. Both of these effects mean that EXAFS is dominated by events in which the photoelectron is scattered only once and then returns to the X-ray absorbing atom or, in some case, by a limited number of multiple scattering paths.

In the XANES region, the scattering of photoelectron away from the forward and backward direction is much stronger, and is coupled with the fact that the mean free path is much greater since the inelastic losses are weaker. We can say that the XANES is dominated by multiple scattering and its theoretical description is more difficult.

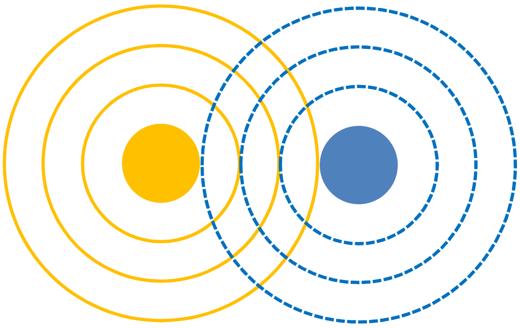

Figure 1.3: Image of outgoing photoelectron wave shown in solid line from X-ray absorbing atom (yellow circle) and scattering wave shown in dashed line by neighboring atom (blue circle).

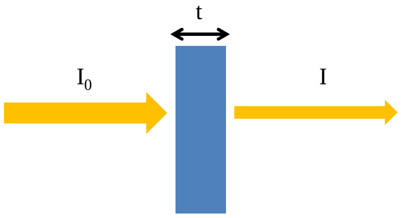

Figure 1.4: The typical X-ray absorption spectroscopy measurement for transmission mode: $I_0$ and I are measured intensities of X-ray, and *t* is the thickness of sample.

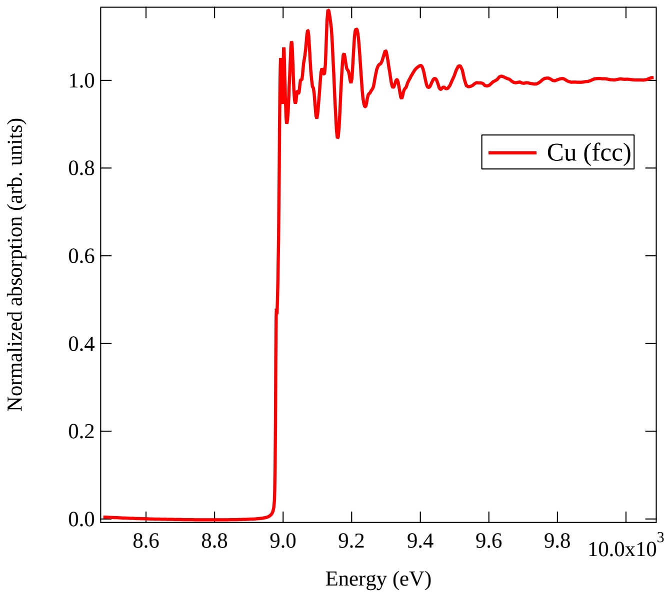

Figure 1.5: Cu K-edge XAFS spectrum of fcc copper.

# Chapter 2

# Theory

## 2.1 Multiple scattering XANES formula

The X-ray absorption intensity $I(\omega)$ for photon energy $\omega$ is approximately described by

$$I(\omega) = -\frac{1}{\pi}\mathrm{Im}\left\langle \phi_{\mathrm{c}} \,\middle|\, \Delta^{\dagger}\mathrm{g}(\epsilon)\Delta \,\middle|\, \phi_{\mathrm{c}} \right\rangle . \tag{2.1}$$

Here $g(\epsilon)$ is Green's function and $\Delta$ is electron-photon interaction operator. Core orbital is strongly localized near nucleus then it is sufficient to consider the following expansion of $g(\epsilon)$,

$$g(\epsilon) = g_0(\epsilon) + \sum_{\alpha} g_0(\epsilon)t_{\alpha}g_0(\epsilon) + \sum_{\alpha\neq\beta} g_0(\epsilon)t_{\alpha}g_0(\epsilon)t_{\beta}g_0(\epsilon) + \ldots \tag{2.2}$$

where $g_0$ is described by

$$g_0 = \frac{1}{\epsilon - T_e + i\eta} \tag{2.3}$$

and we define $g_A$ as follows

$$g_A = g_0 + g_0t_Ag_0 \tag{2.4}$$

First, we consider the X-ray absorption intensity without scattering. In this case, the X-ray absorption intensity can be described as follows,

$$I(\omega) = -\frac{1}{\pi}\mathrm{Im}\left\langle \phi_{\mathrm{c}} \,\middle|\, \Delta^{\dagger}\mathrm{g_A}(\epsilon)\Delta \,\middle|\, \phi_{\mathrm{c}} \right\rangle \tag{2.5}$$

where $g_A$ is Green's function described by

$$\begin{aligned} g_A(\omega) &= [\omega - h_0 - \Sigma_0 + i\eta]^{-1} \\ &= [\omega - h_0 - \Sigma_0 + i\eta]^{-1}\left(\sum_m |\phi_m\rangle\langle\phi_m| + \int \left|\Psi_{\boldsymbol{p}}^-\right\rangle d\boldsymbol{p}\left\langle\Psi_{\boldsymbol{p}}^-\right|\right) \\ &\simeq \int \frac{\left|\Psi_{\boldsymbol{p}}^-\right\rangle d\boldsymbol{p}\left\langle\Psi_{\boldsymbol{p}}^-\right|}{\omega - \epsilon_p + i\eta}. \end{aligned} \tag{2.6}$$

Here we assume the eigenvalue equation

$$(h_0 - \Sigma_0(E_0^c + \omega))\Psi_{\boldsymbol{p}}^- \approx \epsilon\Psi_{\boldsymbol{p}}^- \tag{2.7}$$

The integral of $\boldsymbol{p}$ in equation (2.6) is large when $\epsilon \approx \omega$. Thus, we can approximate $\Sigma_0(E_0^c + \omega) \approx \Sigma_0(E_0^c + \epsilon_p)$. $\Psi_{\boldsymbol{p}}^-(\boldsymbol{r})$ is photoelectron wave function described by,

$$\Psi_{\boldsymbol{p}}^- = \left\langle \boldsymbol{r} \middle| \Psi_{\boldsymbol{p}}^- \right\rangle = \sqrt{\frac{2}{\pi}}\sum_L i^l R_l(r) Y_L(\hat{\boldsymbol{r}}) e^{-i\delta_l} Y_L(\hat{\boldsymbol{p}}). \tag{2.8}$$

Inserting equation (2.8) into equation (2.6),

$$\begin{aligned} g_A(\boldsymbol{r}, \boldsymbol{r}'; \omega) &\approx \frac{2}{\pi}\int d\boldsymbol{p} \sum_{LL'} \frac{i^{l-l'}}{\omega - \epsilon_p + i\eta} R_l(r) R_l(r') Y_L(\hat{\boldsymbol{r}}) Y_{L'}^*(\hat{\boldsymbol{r}}) e^{i(\delta_l - \delta_{l'})} Y_L^*(\hat{\boldsymbol{p}}) Y_{L'}(\hat{\boldsymbol{p}}) \\ &= \frac{2}{\pi}\sum_L \int_0^\infty p^2 dp \frac{1}{\omega - \epsilon_p + i\eta} R_l(pr) R_l(pr') Y_L(\hat{\boldsymbol{r}}) Y_{L'}^*(\hat{\boldsymbol{r}}) \end{aligned} \tag{2.9}$$

The X-ray absorption intensity is obtained by substituting equation (2.9) into equation (2.5),

$$\begin{aligned} I(\omega) &\approx -\frac{4}{\pi^2}\sum_L \int_0^\infty dp\{-\pi\delta(k^2 - p^2)p^2\} \left|\left\langle \phi_c \middle| \Delta^\dagger \middle| R_l Y_L \right\rangle\right|^2 \\ &= \frac{2k}{\pi}\sum_L \left|\left\langle \phi_c \middle| \Delta^\dagger \middle| R_l Y_L \right\rangle\right|^2. \end{aligned} \tag{2.10}$$

If the incident X-ray is polarized along the z-axis, electron-photon operator $\Delta$ is described

$$\Delta \propto z = \sqrt{\frac{4\pi}{3}} r Y_{10}(\hat{\boldsymbol{r}}). \tag{2.11}$$

Thus, the matrix element in equation (2.10) is described as follows,

$$\begin{aligned}\langle R_l Y_L \,|\, z \,|\, \phi_c\rangle &= \sqrt{\frac{4\pi}{3}}\int R_l(kr)R_{l_c}(r)r^3 dr G(L_c 10|L) \\ &= \sqrt{\frac{4\pi}{3}}\rho_c(l)G(L_c 10|L). \end{aligned}\tag{2.12}$$

Here $\rho_c(l)$ is radial dipole integral described as

$$\rho_c(l) = \int R_l(kr)R_{l_c}(r)r^3 dr \tag{2.13}$$

and $G(LL'|L'')$ are defined as the Gaunt integral described as

$$G(LL'|L'') = \int Y_L(\hat{\boldsymbol{r}})Y_{L'}(\hat{\boldsymbol{r}})Y^*_{L''}(\hat{\boldsymbol{r}}). \tag{2.14}$$

From the selection rule of the Gaunt integral, $l$ is restricted to $l = l_c \pm 1$.

Therefore, X-ray absorption intensity can obtained from equation (2.10) and equation(2.12),

$$I(\omega) = \frac{8k}{3}\sum_L \rho_c(l)^2 G(L_c 10|L)^2. \tag{2.15}$$

We can calculate the summation in equation (2.15) as follows,

$$\sum_L \rho_c(l)^2 G(L_c 10|L) = \sum_l \rho_c(l)^2 \frac{3(2l_c+1)}{4\pi(2l+1)}\langle l_c 010\,|\,l\rangle^2 \sum_m \langle L_c 10\,|\,L\rangle^2 . \tag{2.16}$$

For example, if $l_c$ is 0, $m$ is restricted to 0, then the summation can be written as

$$\rho_c(1)^2 \frac{1}{4\pi}\langle 0010\,|\,1\rangle^4 = \frac{1}{4\pi}\rho_c(1)^2. \tag{2.17}$$

Thus, equation (2.15) can be described as follows,

$$I(\omega) = \frac{2k}{3\pi}\rho_c(1)^2 \tag{2.18}$$

Hereafter, we consider the scattering terms. At first, we evaluate single scattering term $\mathrm{Im}\left\langle \phi_{\mathrm{c}} \,\middle|\, \Delta^\dagger \mathrm{g_A}(\omega)\mathrm{t}_\alpha \mathrm{g_A}(\omega)\Delta \,\middle|\, \phi_{\mathrm{c}}\right\rangle$. The following angular momentum expansion is applied when $\boldsymbol{r} \in \alpha$, $\boldsymbol{r'} \in A$,

$$g_A(\boldsymbol{r},\boldsymbol{r}';k) = -2ik\sum_L h_l^{(1)}(kr)\exp(i\delta_l^A)R_l(kr')Y_L(\hat{\boldsymbol{r}})Y_L^*(\hat{\boldsymbol{r}'}) \tag{2.19}$$

where $\delta_l^A$ is phase shift of $l$-th partial wave at site $A$. We assume the core orbital as

$$\phi_c(r) = R_c(r)Y_{L_c}(\hat{\boldsymbol{r}}) \tag{2.20}$$

then the single scattering term can be rewritten as follows,

$$\begin{aligned} &\left\langle \phi_c \,\middle|\, \Delta^\dagger g_A(\omega)t_\alpha g_A(\omega)\Delta \,\middle|\, \phi_c \right\rangle \\ = \;& \frac{4\pi}{3}\int \phi_c^*(\hat{\boldsymbol{r}})rY_{10}(\hat{\boldsymbol{r}})g_A(\boldsymbol{r},\boldsymbol{r}')t_\alpha(\boldsymbol{r}',\boldsymbol{r}'')g_A(\boldsymbol{r}'',\boldsymbol{r}''') \\ & \times r'''Y_{10}(\hat{\boldsymbol{r}'''})\phi_c(\hat{\boldsymbol{r}'''})d\boldsymbol{r}d\boldsymbol{r}''' \end{aligned} \tag{2.21}$$

Note that $\boldsymbol{r},\boldsymbol{r}''' \in A$, $\boldsymbol{r}',\boldsymbol{r}'' \in \alpha$ and perform integration for parameter $\boldsymbol{r}$ with substituting equation (2.19) into equation (2.21).

$$\begin{aligned} & e^{i\delta_l^A}\int \phi_c^*(\boldsymbol{r})rY_{10}(\hat{\boldsymbol{r}'})R_l(kr)Y_L^*(\hat{\boldsymbol{r}})d\boldsymbol{r} \\ = \;& e^{i\delta_l^A}\int_0^\infty r^3R_{l_c}R_l(kr)drG(L_cL|10) \\ = \;& e^{i\delta_l^A}\rho(l_c;l)G(L_cL|10) \quad . \end{aligned} \tag{2.22}$$

From the integration of $\boldsymbol{r}'''$ we can obtain

$$e^{i\delta_{l'}^A}\rho(l_c;l')G(L_c10|L'). \tag{2.23}$$

Therefore, the integration of the equation (2.21) can be rewritten as follows,

$$\begin{aligned} (-2ik)^2\sum_{LL'}\int_0^\infty h_l^{(1)}(kr')Y_L(\hat{\boldsymbol{r}'})t_\alpha(\boldsymbol{r}',\boldsymbol{r}'')h_{l'}^{(1)}(kr'')Y_{L'}(\hat{\boldsymbol{r}''})d\boldsymbol{r}'d\boldsymbol{r}'' \\ \times\rho(l_c;l)\rho(l_c;l')G(L_cL|10)G(L_c10|L'). \end{aligned} \tag{2.24}$$

For the spherical symmetric potential, $t_\alpha(\boldsymbol{r}',\boldsymbol{r}'')$ is described by

$$t_\alpha(\boldsymbol{r}',\boldsymbol{r}'') = \sum_{L_1} t_{l_1}(r'_\alpha, r''_\alpha)Y_{L_1}(\hat{\boldsymbol{r}'}_\alpha)Y_{L_1}^*(\hat{\boldsymbol{r}''}_\alpha). \tag{2.25}$$

The integration of both $\boldsymbol{r},\boldsymbol{r}''$ in equation (2.21) is described from the nucleus of the site $A$, it needs to move the origin from the site $A$ to the site $\alpha$. From the origin shift formula,

$$-ikh_l^{(1)}(k|\boldsymbol{r}_\alpha + \boldsymbol{R}_\alpha|)Y_L(\widehat{\boldsymbol{r}_\alpha + \boldsymbol{R}_\alpha}) = \sum_{L_2} G_{L_2L}(\boldsymbol{R}_\alpha)J_{L_2}(k;\boldsymbol{r}_\alpha)i^{l-l_2} \tag{2.26}$$

where $J_{L_2}$ is

$$J_{L_2} = j_{L_2}(k;\boldsymbol{r}_\alpha)Y_{L_2}(\hat{\boldsymbol{r}}_\alpha). \tag{2.27}$$

Inserting equation (2.26) into equation (2.24),

$$\begin{aligned} & 4\sum_{LL'}\sum_{L_2L'_2}\sum_{L_1} G_{L_2L}(\boldsymbol{R}_\alpha)i^{l_2-l}G_{L'_2L'}(\boldsymbol{R}_\alpha)i^{l'_2-l'}e^{i(\delta_l^A+\delta_{l'}^A)}\rho(l_c;l)\rho(l_c;l')G(L_cL|10)G(L_c10|L') \\ \times & \int d\boldsymbol{r}'d\boldsymbol{r}''J_{l_2}(k\boldsymbol{r}'_\alpha)J_{l'_2}(k\boldsymbol{r}'_\alpha)t_{l_1}(\boldsymbol{r}'_\alpha,\boldsymbol{r}''_\alpha)Y_{L_1}(\hat{\boldsymbol{r}}'_\alpha)Y^*_{L_1}(\hat{\boldsymbol{r}}''_\alpha). \end{aligned} \tag{2.28}$$

By substituting equation (2.25) into the equation (2.28),

$$\begin{aligned} & \int d\boldsymbol{r}'d\boldsymbol{r}''J_{l_2}(k\boldsymbol{r}'_\alpha)J_{l'_2}(k\boldsymbol{r}'_\alpha)t_{l_1}(\boldsymbol{r}'_\alpha,\boldsymbol{r}''_\alpha)Y_{L_1}(\hat{\boldsymbol{r}}'_\alpha)Y^*_{L_1}(\hat{\boldsymbol{r}}''_\alpha) \\ = \; & \delta_{\bar{L}_2L_1}\delta_{L'_2L_1}(-1)^{m_1}\int j_{l_1}(kr'_\alpha)j_{l'_1}(kr''_\alpha)t_{l_1}(r'_\alpha,r''_\alpha)r'_\alpha r''^2_\alpha dr'_\alpha dr''_\alpha \\ = \; & \delta_{\bar{L}_2L_1}\delta_{L'_2L_1}(-1)^{m_1}\frac{t^\alpha_{l_1}(k)}{2} \quad . \end{aligned} \tag{2.29}$$

Here $\bar{L_2} = (l_2,-m_2)$ and,

$$t^\alpha_{l_1}(k) = -\frac{1}{2ik}\left(e^{2i\delta_l^\alpha}-1\right). \tag{2.30}$$

From equation (2.29) and (2.30), equation (2.28) can be rewritten as follows,

$$\begin{aligned} & 2\sum_{LL'L'''} G_{l'',-m'',L}(\boldsymbol{R}_\alpha)(-1)^{m''}i^{l''-l}G_{L'',L'}(\boldsymbol{R}_\alpha)i^{l''-l'} \\ & \times e^{i(\delta_l^A+\delta_{l'}^A)}\rho(l_c;l)\rho(l_c;l')G(L_cL|10)G(L_c10|L')t^\alpha_{l''}(k). \end{aligned} \tag{2.31}$$

We use the following relation in order to simplify the equation (2.31),

$$G_{l'',-m'',L}(\boldsymbol{R}_\alpha) = (-1)^{l+l''m-m''}G_{l,-m,L''}(-\boldsymbol{R}_\alpha). \tag{2.32}$$

Inserting equation (2.32) into equation (2.31), we can obtain

$$\begin{aligned} & 2\textstyle\sum_{LL'} i^{l-l'}(-1)^m\rho(l_c;l)\rho(l_c;l')G(L_cL|10)G(L_c10|L') \\ & \quad \times e^{i(\delta_l^A+\delta_{l'}^A)}\textstyle\sum_{L''} G_{l'',-m'',L}(\boldsymbol{R}_\alpha)t^\alpha_{l''}(k)G_{L'',L'}(\boldsymbol{R}_\alpha) \\ = \; & 2\textstyle\sum_{LL'} i^{l-l'}(-1)^m\rho(l_c;l)\rho(l_c;l')G(L_c10|L)G(L_c10|L') \\ & \quad \times e^{i(\delta_l^A+\delta_{l'}^A)}\textstyle\sum_{L''} G_{L,L''}(\boldsymbol{R}_\alpha)t^\alpha_{l''}(k)G_{L'',L'}(\boldsymbol{R}_\alpha) \end{aligned} \tag{2.33}$$

Therefore the single scattering term is described as

$$\begin{aligned}\left\langle \phi_c \middle| \Delta^\dagger g_A(\omega) t_\alpha g_A(\omega) \Delta \middle| \phi_c \right\rangle &= \frac{8\pi}{3} \sum_{LL'} i^{l-l'} e^{i(\delta_l^A+\delta_{l'}^A)} \rho_c(l)\rho_c(l') G(L_c10|L) G(L_c10|L') \\ &\times \sum_{L''} G_{LL''}(-\boldsymbol{R}_\alpha) t^\alpha_{l''} G_{L''L'}(\boldsymbol{R}_\alpha). \qquad (2.34)\end{aligned}$$

In the same way, the *n*th order of multiple scattering term is given by

$$\begin{aligned}&\frac{8\pi}{3} \sum_{LL'} i^{l-l'} e^{i(\delta_l^A+\delta_{l'}^A)} \rho_c(l)\rho_c(l') G(L_c10|L) G(L_c10|L') \\ \times \sum_{\alpha_1 \ldots \alpha_n} \sum_{L_1 \ldots L_n} &G_{LL_n}(-\boldsymbol{R}_{\alpha_n}) t^{\alpha_n}_{l_n}(k) G_{L_nL'_n}(\boldsymbol{R}_{\alpha_n} - \boldsymbol{R}_{\alpha_{n-1}}) t^{\alpha_{n-1}}_{l_{n-1}}(k) \ldots \times G_{L'_1L'}(\boldsymbol{R}_{\alpha_1}). \quad (2.35)\end{aligned}$$

Here we define the matrix $X$

$$X^{\alpha\beta}_{LL'} = t^\alpha_l G_{LL'}(\boldsymbol{R}_\alpha - \boldsymbol{R}_\beta)(1 - \delta_{\alpha\beta}). \qquad (2.36)$$

The summation of $\sum_{\alpha_1 \ldots \alpha_n} \sum_{L_1 \ldots L_n}$ in the equation (2.35) can be simplified by use of equation (2.36)

$$\begin{aligned}&\sum_{\alpha_n} \sum_{L_n} G^{A\alpha_n}_{LL_n} (X^n)^{\alpha_n A}_{L_n L} && (2.37) \\ = \ &GX + GX^2 + GX^3 + \ldots + GX^n + \ldots = GX(1-X)^{-1}. && (2.38)\end{aligned}$$

Each terms in the equation (2.38) represent single, double, . . . scattering effect in X-ray absorption intensity. Here we add $[G]^{AA}_{LL'} = 0$, and then the equation (2.38) can be rewrite as followings

$$G(1 + X + X^2 + X^3 + \ldots) = G(1 - X)^{-1}. \qquad (2.39)$$

Therefore, the representation of the X-ray absorption intensity including full multiple scattering is described by

$$\begin{aligned}I(\omega) &= -\frac{8}{3} \mathrm{Im} \Bigg\{ \sum_{\mathrm{LL'}} \mathrm{i}^{\mathrm{l-l'}} \mathrm{e}^{\mathrm{i}(\delta_{\mathrm{l}}^{\mathrm{A}}+\delta_{\mathrm{l'}}^{\mathrm{A}})} \rho_{\mathrm{c}}(\mathrm{l}) \rho_{\mathrm{c}}(\mathrm{l'}) \\ &\times G(L_c10|L) G(L_c10|L') (t^{-1})^{AA}_{LL'} [(1-X)^{-1}]^{AA}_{LL'} \Bigg\} \qquad (2.40)\end{aligned}$$

where the relations $X = tG$ and $t^{-1} + G(1-X)^{-1} = t^{-1}(1-X)^{-1}$ are used. The equation (2.40) include infinite order of the scattering inside the cluster.

The dimension of the matrix X is described by

$$n(l_{max} + 1)^2 \tag{2.41}$$

where $n$ is the number of atoms inside the cluster and $l_{max}$ is the maximum partial wave $l$ we should consider. For example, the cluster which consist of 100 atoms and consider the partial wave up to $f$ wave, the dimension of the matrix X amount to 1600. The direct calculation of the matrix X is difficult due to the large dimension. In order to calculate the inverse matrix of the X, we divide the matrix X into small matrix as followings,

$$[G(1 - X)^{-1}]^{A,A}_{L,L'} = \sum_{\alpha,L''} G^{A\alpha}_{LL''}[(1 - X)^{-1}]^{A\alpha}_{LL''} \tag{2.42}$$

$$(1 - X) = \begin{pmatrix} A & B \\ C & D \end{pmatrix} \tag{2.43}$$

and

$$(1 - X)^{-1} = \begin{pmatrix} U & V \\ S & T \end{pmatrix} \tag{2.44}$$

therefore,

$$\begin{pmatrix} A & B \\ C & D \end{pmatrix}\begin{pmatrix} U & V \\ S & T \end{pmatrix} = \begin{pmatrix} 1_n & 0 \\ 0 & 1_m \end{pmatrix}. \tag{2.45}$$

From the equation (2.45), we can easily obtain simultaneous equation

$$\begin{cases} AU + BS = 1_n \\ AV + BT = 0 \\ CU + DS = 0 \\ CV + DT = 1_m \end{cases} \tag{2.46}$$

The matrix A is described about X-ray absorbing atom and the matrix D is described about the scattering of the other atoms. From the third of the equation (2.46),

$$S = -D^{-1}CU \tag{2.47}$$

and then substitute into first of the equation (2.46),

$$U = (A - BD^{-1}C)^{-1} \tag{2.48}$$

Substitute (2.48) into (2.47)

$$S = -D^{-1}C(A - BD^{-1}C)^{-1}. \tag{2.49}$$

## 2.2 Single scattering formulas for EXAFS

Extended X-ray absorption fine structure (EXAFS) spectra which are higher energy region rather than XANES contain the information on the geometrical structure. The EXAFS function is defined as

$$\chi(k) = \frac{\mu(E) - \mu_0(E)}{\mu_0(E)} \tag{2.50}$$

where $\mu(E)$ is observed absorption coefficient and $\mu_0(E)$ is smooth background absorption of isolated atom. $\chi(k)$ is a function of photoelectron wavenumber $k$ which is defined by

$$k = \sqrt{\frac{2m}{\hbar^2}(E - E_0)} \tag{2.51}$$

where $E_0$ is absorption edge energy, $m$ is electron mass. EXAFS function $\chi(k)$ is described by single scattering theory

$$\chi(k) = S_0^2 \sum_j \frac{N_j f_j(k)}{kR_j^2} \exp(-2\sigma_j^2 k^2) \exp(-2R_j/\lambda_j(k)) \sin(2kR_j + \phi_j(k)) \tag{2.52}$$

where $S_0^2$ is reduction factor due to the many-body effect, $N$ is coordination number, $R$ is distance to neighboring atom and $\sigma^2$ is caused by thermal vibration and geometric disorder in the neighbor distance. $\exp(-2\sigma_j^2 k^2)$ is called Debye-Waller factor [9, 10]. $\phi$ is scattering phase shift and $\lambda$ is mean free path of photoelectron that is how far the photoelectron travels before scattering inelastically and before the core hole is filled. The mean free path is typically 5 to 30 Å and depends on the energy of photoelectron. The dependence is called universal curve.

The EXAFS oscillation $\chi(k)$ depends on $\sin(2kR_j)$, the Fourier transformed EXAFS spectrum has peaks corresponding to the distances of the neighboring atom. However, the effect of phase shift $\phi(k)$, the peak positions are shorter than actual distance. In order to obtain the structural information from Fourier transformed EXAFS spectra, the curve fitting is often used. The curve fitting gives us the structural information about $N$, $R$ and $\sigma^2$.

# Chapter 3

# Analysis of Cu K-edge XAFS spectra of Cu(II) bound to human COMMD protein

## 3.1 COMMD protein

Protein is one of the most important component in all living organisms. Proteins consist of linear polymers built from series of 20 L-amino acids and play a important role including maintaining body tissue, catalyzing metabolic reaction, transporting molecules, antibody effect, cell multiplication, DNA replicating, responding to stimuli, etc.. The function of protein strongly depends on their three dimensional structure. Thus the understanding of three dimensional protein structure is important for clarifying the function of the protein.

Copper is an essential trace element for living things. The roles of this element are synthesizing protein and enzyme, transporting electrons and oxygen, antibody effect, etc. [11, 12]. But an accumulation of copper causes Wilson disease, cirrhosis of the liver, abnormal retina[13]. It is also related to gene and protein mutation or neurodegenerative diseases such as Parkinson, Alzheimer, Creutzfeldt-Jacob or Bovine Spongiform Encephalopathy (BSE) disease[14]. Deficiency of copper causes growth retardation called Menkes disease, i.e. peculiar hair, focal cerebral and cerebellar degeneration[15]. Understanding the copper metabolism mechanism is important to prevent these diseases.

Copper metabolism Murr1 (mouse U2af1-rs1 region1) domain (COMMD) proteins are considered to be related to copper metabolism in organisms. COMMD protein is defined by presence of COMM domain. This domain consists of 70-85 amino acid residues near C-terminal side and is predicted to form $\beta$-sheet structure [16, 17]. Each COMMD protein member is characterized by specific amino acid sequence at the N-terminal side. In human, the COMMD protein family consists of 10 members [16]. Human COMMD1, COMMD6 and COMMD7, which we focus on in this thesis, belong to COMMD protein family.

COMMD1, which has 190 amino acid residues with molecular mass of 21 kDa and is related to copper metabolism and regulation of transcription factor NF-$\kappa$B, has been most studied [17].

MAAGE LEGGK PLSGL LNALA QDTFH GYPGI TEELL
RSQLY PEVPP EEFRP FLAKM RGILK SIASA DMDFN
QLEAF LTAQT KKQGG ITSDQ AAVIS KFWKS HKTKI
RESLM NQSRW NSGLR GLSWR VDGKS QSRHS AQIHT
PVAII ELELG KYGQE SEFLC LEFDE VKVNQ ILKTL
SEVEE SISTL ISQPN

Figure 3.1: Amino acid sequence of human COMMD1 protein.

COMMD1 binds to copper(II) ion *in vitro* in 1:1 molar ratio [17, 18]. Although the N-terminal tertiary structure of COMMD1 has been reported [2], its full length structure and which residues bind a copper(II) ion is not known.

According to Narindrasorasak *et al.*, the fragment of COMMD1 which consists of the 60 to 154 amino acid residues in COMMD1 bind a copper(II) ion [17]. Sommerhalter *et al.* have shown that the 1 to 108 amino acid residues from N-terminal do not bind a copper(II) ion [2]. Therefore, the 109 to 154 amino acid residues in COMMD1 bind a copper(II) ion.

COMMD6 which has 85 amino acid residues with molecular mass 9.6 kDa consists almost solely of the COMM domain. COMMD6 is known to interact with COMMD1 [19]. Structural information beyond the amino acid sequence has not been reported for COMMD6.

Only the amino acid sequence is known about the COMMD7, which has 200 amino acid residues with molecular mass 22.5 kDa. Recently we have found that COMMD6 and COMMD7 also bind to copper(II) ion [18].

## 3.2 Experimental

The expression and purification of COMMD1, COMMD6 and COMMD7 will be reported in detail elsewhere [18]. In here, we describe the process briefly. A strain of *Escherichia coli* BL21 (DE3) was transformed by inserting cDNA of COMMD proteins into the expression vector pET32b(+) at NcoI-EcoRI site. 1 mM of Isopropyl $\beta$-D-1-thiogalactopyranoside was added to culture solution

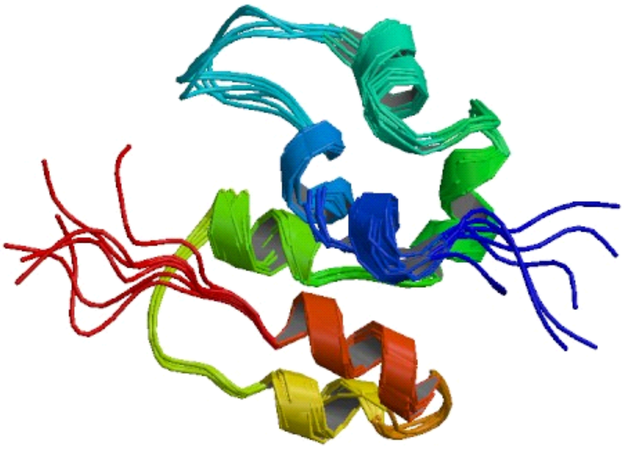

Figure 3.2: N-terminal structure of COMMD1 reported by Ref. [2].

MEASS EPPLD AKSDV TNQLV DFQWK LGMAV SSDTCRS
LKYPY VAVML KVADH SGQVK TKCFE MTIPQ FQNFY
RQFKE IAAVI ETV

Figure 3.3: Amino acid sequence of human COMMD6 protein.

of the *Escherichia coli*. Expression of proteins was induced by keeping the solution at 37 °C for 16 hours. Produced COMMD1, COMMD6 and COMMD7 without tags were dissolved in Tris buffer (20 mM Tris, 100 mM NaCl, pH 7.5). When copper(II) ions are introduced, the solution contains Cu-COMMD protein complex and $\mathrm{Cu[H_2O]_6^{2+}}$ complex which are in equilibrium and XAFS spectra inevitably have contributions from both components. Therefore, it is desirable to separate these components from observed XAFS spectra in order to analyze the structure of Cu-COMMD protein complex.

Factor analysis is suitable to this purpose. Factor analysis requires a series of spectra from samples with different concentration of the constituents in order to separate pure spectrum components. We prepared samples whose concentration

MGRLH CTEDP VPEAV GGDMQ QLNQL GAQQF SALTE
VLFHF LTEQK EVERF LAQLS EFATT NQISL GSLRS
IVKSL LLVPN GALKK SLTAK QVQAD FITLG LSEEK
ATYFS EKWKQ NTPTL ARWAI GQTLM INQLI DMEWK
FGVTS GSSEL EKVGS IFLQL KLVVK KGNQT KNVYI
ELTLP QFYSF LHEME RVRTS MECFC

Figure 3.4: Amino acid sequence of human COMMD7 protein.

of either copper(II) ion or COMMD protein is different for this purpose. For COMMD1, we prepared three samples with protein concentration of 1 mM. The concentrations of copper(II) ion for these samples were 40 $\mu$M, 200 $\mu$M, 400 $\mu$M. For COMMD6, we prepared three samples with protein concentration of 1.1 mM, 1.4 mM, 1.8 mM. The concentration of copper(II) ion was 1 mM in all COMMD6 samples. For COMMD7, we prepared three samples with protein concentration of 0.5 mM, 1.0 mM, 1.5 mM. The concentration of copper(II) ion was 1 mM in all COMMD7 samples. 1 mM $CuSO_4$ aqueous solution was also measured as a reference.

The Cu K-edge XAFS measurements were performed at BL-12C of Photon Factory, KEK. The beamline is equipped with a Si (111) double crystal monochromator. X-ray absorption spectra were recorded in the fluorescence mode using a 19 element solid state detector [20]. The signals were corrected for the counting loss due to the dead time of detection system according to the method described in Ref. [20]. All the samples were sealed in sample cells which have polyimide windows. The samples which contain COMMD protein were frozen by liquid nitrogen prior to the measurements in order to minimize the damage due to the x-ray irradiation. The samples were kept at 100 K using a closed cycle He cryostat during the measurements. We also measured other reference copper(II) complexes.

## 3.3 Facter analysis

In the measured samples, Cu-COMMD protein and $Cu[H_2O]_6^{2+}$ complexes are in equilibrium and the experimental XANES spectra are mixtures of these two components. It is necessary to separate these components from the observed XANES spectra in order to analyze the pure spectral components. We use a multivariate curve resolution method which is called alternating least squares (ALS) method [21, 22, 23]. In ALS method, observed spectral data are arranged in a matrix **D** with one spectrum per row. The objective is to decompose the matrix **D** into the product of concentration profile **C** and pure chemical component spectra **A**,

$$\mathbf{D} = \mathbf{C}\mathbf{A}. \tag{3.1}$$

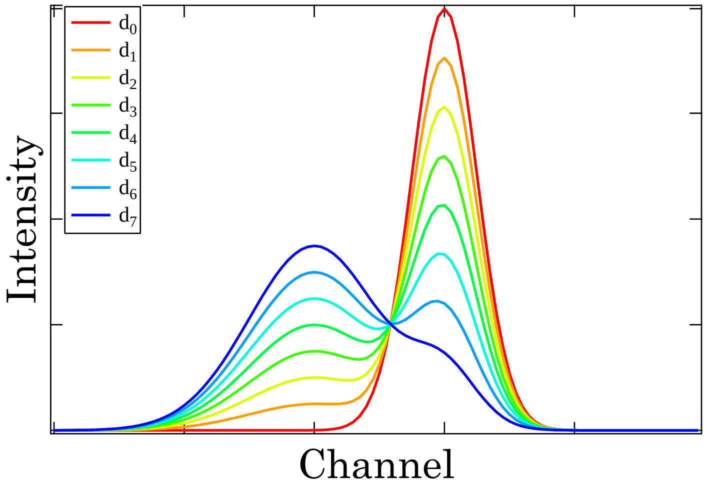

Figure 3.5: Model spectra of Chemometrics

The number of rows and columns of **C** corresponds to the number of the measured spectral data and the number of the components, respectively. The number of rows and columns of **A** corresponds to the number of the components and the number of data points in each spectrum. We use the constraint that the both concentrations and intensities of spectra are non-negative to remove the rotational ambiguity. In ALS method, we first choose an arbitrary initial concentration matrix $\mathbf{C}_0$ and perform following iterative procedure. In each iterative step, new chemical component spectra $\mathbf{A}_i$ and new concentration profile $\mathbf{C}_{i+1}$ are obtained from the equations,

$$\mathbf{A_i} = \mathbf{C_i^+}\mathbf{D}, \tag{3.2}$$

$$\mathbf{C_{i+1}} = \mathbf{D}\mathbf{A_i^+}, \tag{3.3}$$

where $\mathbf{C}^+$ and $\mathbf{A}^+$ are the pseudoinverses of the matrices **C** and **A**. They are given as $\mathbf{C}^+ = (\mathbf{C^T}\mathbf{C})^{-\mathbf{1}}\mathbf{C^T}$ and $\mathbf{A}^+ = \mathbf{A^T}(\mathbf{A}\mathbf{A^T})^{-\mathbf{1}}$, where $\mathbf{C^T}$ and $\mathbf{A^T}$ are the transposes of **C** and **A**. This procedure is iterated until convergence is achieved. We use the spectrum of $CuSO_4$ aqueous solution as the pure spectrum of $Cu[H_2O]_6^{2+}$.

## 3.4 Result and Discussion

Figure 3.6 shows the experimental Cu K-edge EXAFS spectra of COMMD1, COMMD6 and COMMD7 samples. Figure 3.7 shows the magnitudes of the Fourier transformed experimental Cu K-edge EXAFS spectra of the COMMD1, COMMD6 and COMMD7 samples, together with the spectrum of $CuSO_4$ aqueous solution as a reference which represents the hydrated copper(II) ion $Cu[H_2O]_6^{2+}$. $k^2$ weighted spectra are Fourier transformed using the k-range of 2-8 $Å^{-1}$. The first peak position corresponds to the distance between copper(II) ion and the nearest atom. Note that the peak positions are at shorter distances than the actual distances due to the scattering phase shift. In the case of $CuSO_4$ aqueous solution, the first peak is due to the oxygen atoms in the water molecules in $Cu[H_2O]_6^{2+}$ complex. For COMMD1 and COMMD6 samples, the first peak position is shifted to larger distance compared to the $Cu[H_2O]_6^{2+}$ complex. On the other hand, COMMD7 samples show the peak at the same distance as $Cu[H_2O]_6^{2+}$. Moreover, there are systematic changes in the longer distance side of the first peak which reflect longer range structure which is characteristic in each Cu-COMMD protein complex. This is in particular apparent in the case of COMMD7 samples. However, it is difficult to unambiguously determine the detailed structure only from these EXAFS spectra because EXAFS contains mainly one dimensional information. Nevertheless the structural models from XANES analysis which will be shown below should be consistent with these EXAFS result.

Figure 3.8 shows the observed Cu K-edge XANES spectra and their decomposition into pure spectral components of Cu-COMMD protein and hydrated copper(II) ion complexes by ALS at each concentration. It can be seen from the figure that good convergence of the ALS method has been achieved for each of the datasets. In order to check the stability of the spectral decomposition, we repeated the procedure with different constraints on the concentration profile. Resulting spectral shapes of the pure component do not change substantially. Therefore the pure spectral component obtained by ALS method can serve as the basis of further analysis while there may be considerable uncertainties in the concentration profile. Figure 3.9 shows the molar fraction obtained by the factor analysis of Cu-COMMD protein and $Cu[H_2O]_6^{2+}$ complexes at each concentration. In the case of COMMD1 sample, the concentration of copper(II) ion is varied while the concentration of the protein is kept at 1 mM. The molar fraction of the Cu-COMMD protein complex is $\sim 1$ at the lowest copper(II) ion concentration and dropped to $\sim 0.7$ at [Cu(II)]=200 $\mu$M where the value already tends to saturate. In the case of COMMD6 and COMMD7 samples, the varied quantity is the concentration of COMMD protein. The concentration of copper(II) ion is fixed at 1 mM. The ratio of Cu-COMMD protein complex increase as the concentration of protein increase and nearly saturate at [COMMD6]=1.4 mM and [COMMD7]=0.5

mM where the value of the molar fraction of the protein bound copper(II) ion is significantly lower than 1. These behaviors do not conform to the simple law of mass action for the 1:1 complex in the dilute limit. Although this might be due to the high concentration of proteins in the samples studied here, we shall not discuss this point further because the measurements have been performed at the low temperature and the molar fraction does not necessarily keep the equilibrium at room temperature. The pure spectral components of the Cu-COMMD protein complexes show significant energy shift of the absorption edge to lower energy for all Cu-COMMD proteins compared with $Cu[H_2O]_6^{2+}$. The amount of the shift is as large as 6 eV which corresponds to a change in the oxidation state from Cu(II) to Cu(0) [24, 25]. In this case, although the oxidation state of copper does not change, charge transfer to the copper ion from the ligands due to the formation of coordination bond together with more effective screening of the core hole when the copper(II) ion is bound to large protein molecule may be responsible for the shift. The shape of XANES spectra around absorption edge of the pure spectral component of COMMD1 and COMMD6 are broad. On the other hand, the main peak of the pure spectral component of COMMD7 is sharp compared with COMMD1 and COMMD6. This indicates that the coordination environment of the copper(II) ion bound to COMMD7 is markedly different from COMMD1 and COMMD6. These pure spectra contain information about the three dimensional structure around the copper(II) ion bound to COMMD proteins. Figure 3.10 shows Cu K-edge XANES spectra of pure Cu-COMMD protein complexes together with reference copper(II) compounds. The coordination of copper(II) in the reference compounds is octahedral ($CuSO_4$ aqueous solution, CuEDTA), four-coordinated planer ($CuSO_4 \cdot 5H_2O$, CuO, Cu(acetylacetonato) and Cu(Phthalocyanine)). We also measured a copper(II) binding protein as a reference. Transferrin is well known as metal binding protein and its binding site of metal ion is also known. Histidine, Tyrosine and Aspartic acid bind copper(II) ion in the case of transferrin. When the small ligands are coordinated, the spectral feature such as shoulder structure is clearly observed. However the large ligands such as amino acid are coordinated, the spectral shape becomes broaden. Therefore the spectral shape does not correspond to the coordination structure. To determine the structure, we construct plausible structural models around the copper(II) ion by first principles molecular orbital calculation and theoretically predict XANES spectra from those models using multiple scattering calculation, which is to be compared with the experiment.

Hereafter, we consider the structural models for Cu-COMMD protein complex. amino acid residues which have sulfur, nitrogen or oxygen in side chain, such as cysteine or histidine, often bind a metal ion in protein because sulfur, nitrogen and oxygen have lone pair and can form coordination bond [12]. In the case of COMMD7, the reductive alkylation of cysteine does not affect the copper(II) binding ability [18] and we can assume cysteine does not bind a copper(II) ion. For copper binding proteins, fourfold coordination is the most common for copper(II) ion [12]. For models which consists of four amino acid residues and a copper(II) ion, we optimize the structures with density functional theory (DFT) calculations (B3LYP/LanL2DZ) using Gaussian09 [26]. Based on the results of structural optimization, multiple scattering XANES calculations are performed and compared with the experimental pure spectra. Most of the models which consist of neutral nonpolar amino acid residues excluding cysteine and methionine do not have stable structure within B3LYP. A few such models, e.g. model which consists of proline, valine, leucine and isoleucine do have stable structure, but none of them reproduced the observed XANES spectra. Although there are models containing acidic amino acid residues, i.e. aspartic acid and glutamic acid which have stable structure, agreement with the XANES spectra was poor. Models which contain amino acid residues with bulky side chains such as lysine, arginine, tryptophan and phenylalanine typically do not have stable structure. Models constructed of polar amino acid residues and basic amino acid residues have stable structure. Figure 3.11 shows the calculated Cu K-edge XANES spectra of various optimized model structures. DE model which consists of aspartic acid (D) and glutamic acid (E) is only constructed acidic amino acid residues. HHCM model consists of histidine (H), cysteine (C) and methionine (M). HKCS model consists of histidine (H), lysine (K), cysteine (C) and serine (S). These three models are close to four-coordinated planer structure. DIVA model which consists of aspartic acid (D), isoleucine (I), valine (V) and alanine (A) is close to tetrahedral coordination. From the comparison between experimental and theoretical XANES calculations using the results of the structural optimization of these models, we conclude the following models most closely reproduce the experimental result.

Figure 3.12 shows the structural models: (a) TYNH model for Cu-COMMD1 protein complex which consists of threonine (T), tyrosine (Y), asparagine (N) and histidine (H). (b) CHMS model for Cu-COMMD6 protein complex which consists of cysteine (C), histidine (H), methionine (M) and serine (S). (c) 2H2M model for Cu-COMMD7 protein complex which consists of two histidines (H) and two methionines (M). In all of these structural models, the copper(II) ion is coordinated by four neighboring atoms. In the TYNH model of Cu-COMMD1 protein complex, the copper(II) ion is coordinated by two nitrogen and two oxygen atoms at distances 2.19 Å (O of threonine), 2.22 Å (O of tyrosine), 2.19 Å (N of asparagine) and 2.28 Å (N of histidine). The structure of the coordination is close to planar. In the CHMS model of Cu-COMMD6 protein complex, the copper(II) ion is coordinated by two sulfur, one oxygen and one nitrogen atoms at distances 2.37 Å (S of cysteine), 2.03 Å (N of histidine), 2.52 Å (S of methionine) and 1.93 Å (O of serine). The structure of the coordination is distorted tetrahedral. In the 2H2M model of Cu-COMMD7 protein complex, the copper(II) ion is coordinated by two nitrogen and two sulfur atoms at distances 2.05 Å (N of histidine), 2.06 Å (N of histidine), 2.54 Å (S of methionine) and 2.65 Å (S of methionine). The structure of the coordination is distorted tetrahedral.

The charge of the copper(II) ion in each model obtained by natural population analysis from Gaussian09 result is +1.00 in TYNH model, +0.69 in CHMS model and +0.79 in 2H2M model while optimized $Cu[H_2O]_6^{2+}$ model gives +1.81. Pavelka *et al*. have reported copper charge of $Cu[(H_2O)_m(H_2S)_n(NH_3)_k]^{2+}$ $(m+n+k=4)$ complexes calculated by DFT (B3PW91/6-31+G(d)) [27]. Katz *et al*. have also reported copper charge of $Cu[(H_2S)_m(NH_3)_n]^{2+}$ $(m+n=4)$ complexes calculated by DFT (MP2/LanL2DZ+d) [12]. Their results showed the clear chemical trend that the charge of copper tends to decrease when the number of coordinated sulfur atom is increased and tends to increase when the number of oxygen atom is increased. The copper charge of our calculation shows similar tendency as their result though the absolute values are significantly smaller by a factor of 1.4 ∼ 1.6 due to the larger ligands which donate electrons more effectively in forming coordination bonds. This may be related to the large shift observed in the XANES spectra.

Figure 3.13 shows the calculated Cu K-edge XANES spectra from these models and the pure spectral component obtained by ALS method. The calculated spectral shape of TYNH model, CHMS model and 2H2M model shows satisfactory agreement with the spectral features of the obtained pure spectra of COMMD1, COMMD6 and COMMD7. Thus, the local structures around copper(II) ion in COMMD protein are well represented by these structural models. Cu(II) K-edge XANES spectra often shows the peak splittings of 6 ∼ 8 eV because of the $d^9$ and $d^{10}$ final states [28, 29]. In the present case, we do not take into account that effect because the observed spectra do not show sharp peaks and it is difficult to assign those final states. Therefore we do not discuss the fine structure in the scale around several eV.

These models also well reproduce the observed EXAFS spectra. Figure 3.14 shows Fourier transformed Cu K-edge EXAFS calculated from the structural models in figure 3.12 using FEFF8 code [30, 31]. In comparing with the experimental data, the calculated spectra have been mixed with calculated spectrum of distorted octahedral model of $Cu[H_2O]_6^{2+}$ complex using the ratio obtained by ALS method in decomposing XANES spectra into pure components (Fig. 3.9). In the EXAFS simulation, we adopted Jahn-Teller distorted octahedral structure for the $Cu[H_2O]_6^{2+}$ component [32, 33, 34, 35] optimized by using Gaussian09 [26]. The optimized distances between copper and oxygen in water molecules are 2.0 Å and 2.2 Å in the equatorial and axial position, respectively. This model reasonably describes the EXAFS of $CuSO_4$ aqueous solution. Multiple scattering paths with effective path length up to 8 Å are included in the EXAFS simulation. The Debye-Waller factor was not necessary because of the complexity of the structural model, which tends to cancell out the EXAFS oscillation corresponding to longer distances without the thermal factor. In the case of TYNH model, the distance disparity in optimized structure is small. Therefore the magnitude of the Fourier transformed EXAFS spectra is larger than the experimental result. In comparing with the experimental data $k^2$ weighted spectra are Fourier transformed using the k-range 2-8 Å$^{-1}$. The experimental EXAFS spectra are mixture of the Cu-COMMD protein complex and $Cu[H_2O]_6^{2+}$ components. The concentration dependence of the Fourier transformed EXAFS spectra is caused by the changes in the relative weight of these two components. In the measured samples, the weight of Cu-COMMD protein complex in EXAFS increases when the concentration of copper(II) ion is decreased (COMMD1, Fig. 3.14 (a)) or COMMD protein concentration is increased (COMMD6 and 7, Fig. 3.14 (b) and (c)). The distance between a copper(II) ion and the nearest atom in structural model of $Cu[H_2O]_6^{2+}$ is shorter than that of the structural models for COMMD proteins. The nearest neighbor atoms are also different. This causes the observed shift in the first peak position in Fourier transformed EXAFS when the weight of the Cu-COMMD protein complex is increased, which is the most apparent in COMMD1 samples. This is well reproduced by the simulation. There is also shoulder structure at the longer distance side of the main peak which is characteristic of each Cu-COMMD protein complex. In the case of COMMD6 and COMMD7, this can be interpreted as related to the distance between copper(II) ion and sulfur atom in cysteine and methionine side chains from the calculation using the structural model. In the case of COMMD1, this represents backscattering from carbon atoms in amino acid which are not directly coordinated to the copper(II) ion. The corresponding structure in the Fourier transformed EXAFS of $CuSO_4$ aqueous solution can be explained as due to interference between contributions from equatorial and axial oxygen atoms in the distorted octahedral model. The structural models and concentration profiles deduced by multiple scattering XANES analysis and factor analysis are thus shown to be able to explain also the EXAFS data including the concentration dependence.

## 3.5 Conclusion

We have performed the factor analysis and subsequent multiple scattering XANES analysis for Cu binding COMMD proteins, COMMD1, COMMD6 and COMMD7. The observed spectra are successfully decomposed into the pure spectral component of Cu-COMMD protein and $Cu[H_2O]_6^{2+}$ complexes by factor analysis. From the combined analysis using first principles molecular orbital calculation and multiple scattering calculation we propose the structural models which reproduce the observed XANES and EXAFS spectra including concentration dependence. In

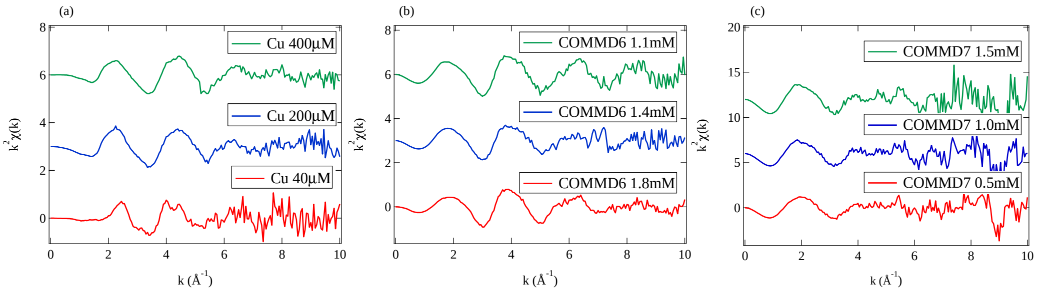

Figure 3.6: Fourier transformed Cu K-edge EXAFS spectra for (a) COMMD1, (b) COMMD6 and (c) COMMD7 samples with different copper(II) ion and protein concentrations. Spectrum of $CuSO_4$ aqueous solution is also shown.

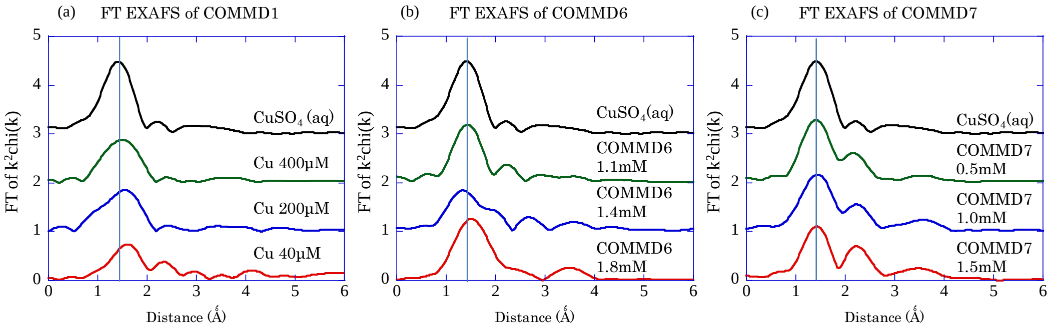

Figure 3.7: Fourier transformed Cu K-edge EXAFS spectra for (a) COMMD1, (b) COMMD6 and (c) COMMD7 samples with different copper(II) ion and protein concentrations. Spectrum of $CuSO_4$ aqueous solution is also shown.

the structural models copper(II) ion is bound to threonine, tyrosine, asparagine and histidine amino acid residues for COMMD1, cysteine, histidine, methionine and serine amino acid residues for COMMD6 and two histidines and two methionines amino acid residues for COMMD7. In these models, the bonding can be interpreted as a coordination bond accompanied by significant electron donation to the copper(II) ion from the ligands, which is reflected in the large shift of the X-ray absorption edge energy. Although all of these COMMD proteins are characterized be the existence of the COMM domain, the copper binding site in the model structure is distinctly different for each COMMD proteins studied here. This also can be seen directly from the pure XANES spectral components decomposed by the factor analysis.

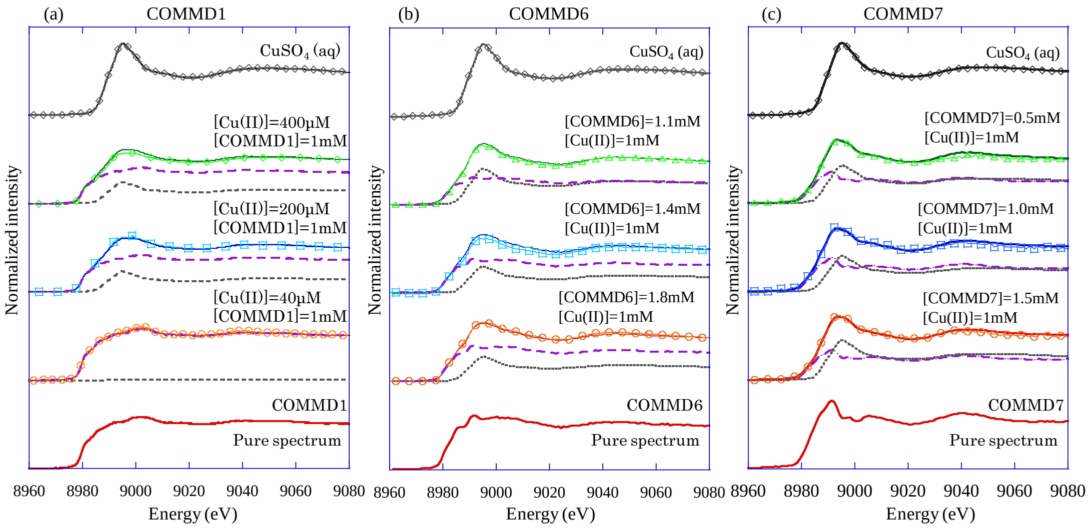

Figure 3.8: Cu K-edge XANES spectra and the result of ALS decomposition of (a) COMMD1, (b) COMMD6 and (c) COMMD7 samples at different concentrations. The observed spectra are shown in solid lines with makers (○ □ △ ◇). At each concentration, ALS decomposed spectra are shown in dashed lines and their sum in solid line. Pure spectral components of Cu-COMMD protein complexes obtained by ALS are shown in solid lines at the bottom of the panels.

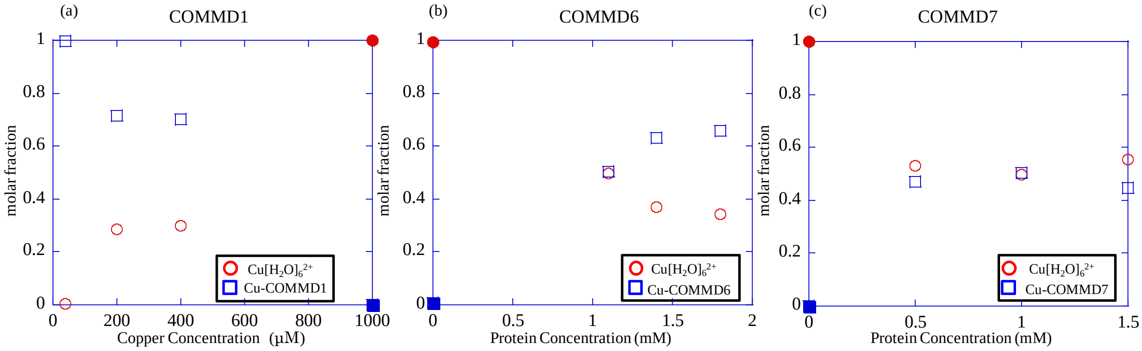

Figure 3.9: Concentration dependence of the molar fraction of (a) Cu-COMMD1, (b) Cu-COMMD6, (c) Cu-COMMD7 and Cu[H$_2$O]$_6^{2+}$ complexes obtained by ALS. Open symbols represent Cu-COMMD protein samples. Closed symbols denote the 1mM CuSO$_4$(aq) sample, which is included in the ALS decomposition of each series as the pure spectral component of Cu[H$_2$O]$_6^{2+}$ complex. In the decomposition the concentration is fixed at 1:0 at that point.

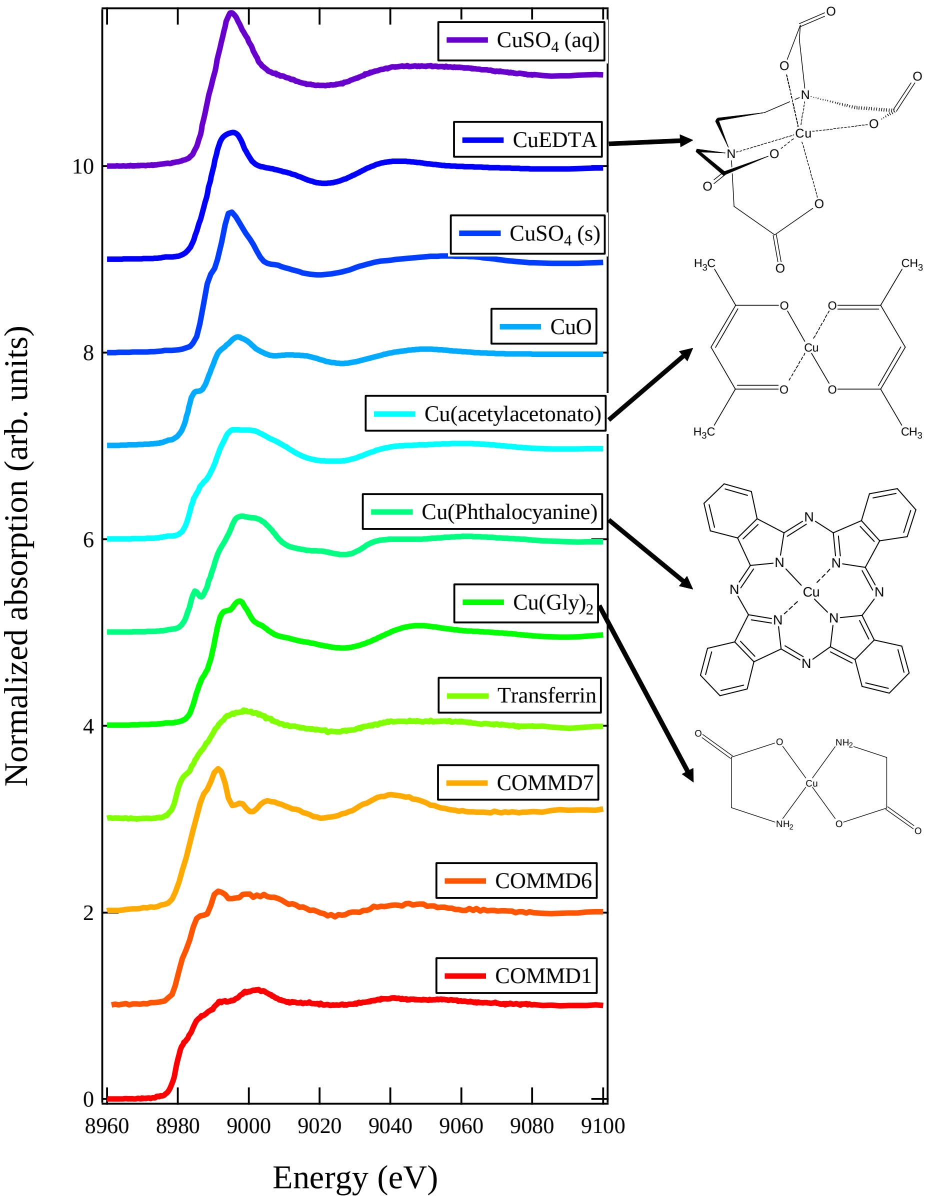

Figure 3.10: Experimental Cu K-edge XANES spectra for various copper(II) compounds.

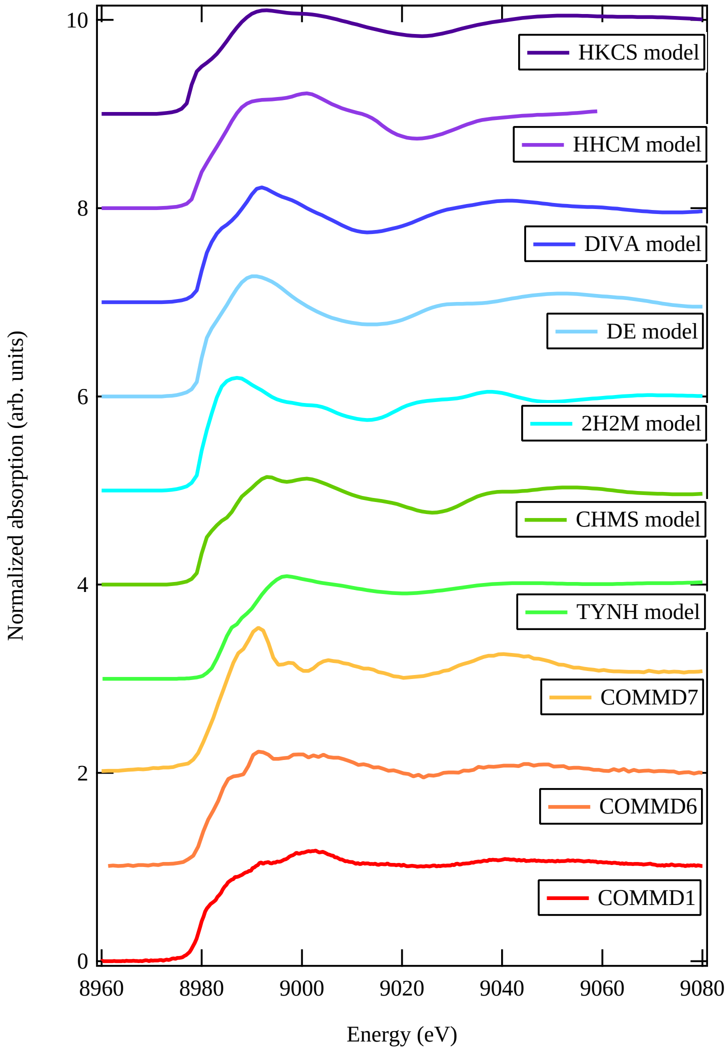

Figure 3.11: Calculated Cu K-edge XANES spectra for various model structures.

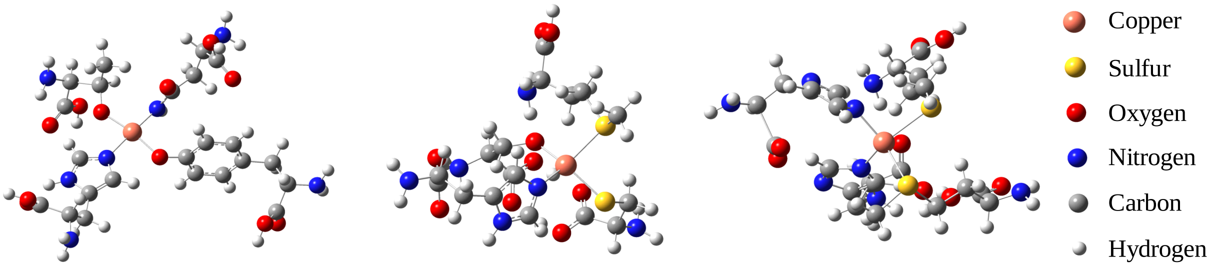

(a) TYNH Model (b) CHMS Model (c) 2H2M Model

Figure 3.12: Model structures optimized by Gaussian09, (a) TYNH model of Cu-COMMD1 protein complex, (b) CHMS model of Cu-COMMD6 protein complex and (c) 2H2M model of Cu-COMMD7 protein complex (see text).

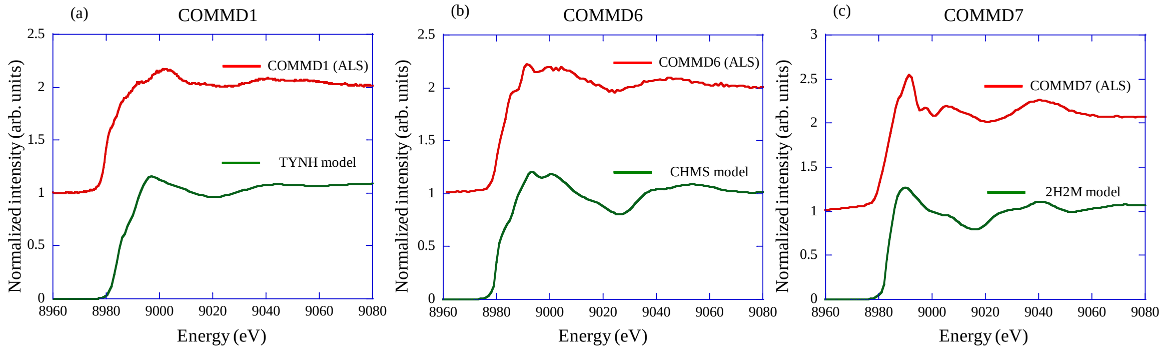

Figure 3.13: Calculated Cu K-edge XANES spectra in (a) TYNH model, (b) CHMS model and (c) 2H2M model compared with the pure spectral components for COMMD1, COMMD6 and COMMD7 obtained by the ALS method.

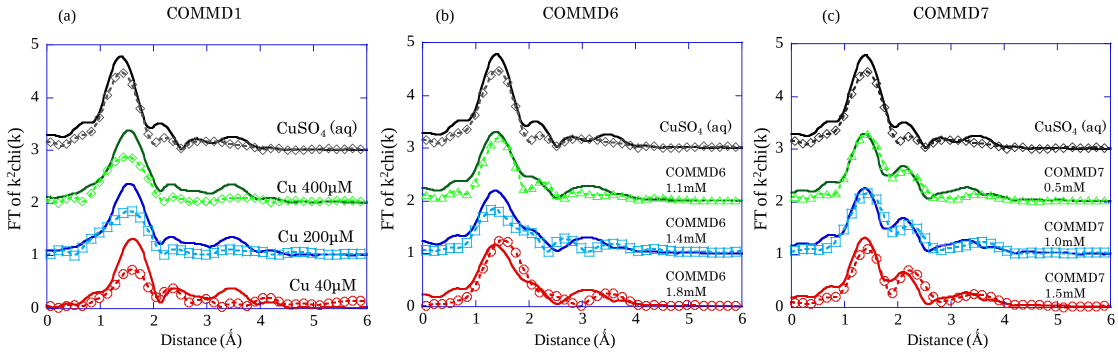

Figure 3.14: Comparison between experimentally observed Cu K-edge EXAFS and calculated EXAFS from the structural models of copper(II) ion bound to COMMD proteins mixed with calculated Cu K-edge EXAFS of $Cu[H_2O]_6^{2+}$ model using with the concentration profile obtained by ALS (a) COMMD1 (TYNH model), (b) COMMD6 (CHMS model), (c) COMMD7 (2H2M model). Calculated spectra are shown in solid lines and the observed spectra are shown in dashed lines with makers (○ □ △ ◇).

# Chapter 4

# Structural analysis of Ligand dependence on TPP[Fe(Pc)$L_2$]$_2$

## 4.1 TPP[Fe(Pc)$L_2$]$_2$

Phthalocyanine (Pc) molecule is vary stable $\pi$-conjugate molecular and can from metal complex with various transition metal. The metal Pc complex has been widely used in dying due to the strong specific absorption in visible region [36, 37]. The Pc molecule is also used for the photoconductor, solar cell, electrochromic display, sensor, etc. due to the strong chemical and thermal stability [38, 39, 40, 41]. The various physical properties of Pc molecules can be produced by controlling central metal, ligand, relative molecular arrangement.

The one-dimensional molecular conductors TPP[Fe(Pc)$L_2$]$_2$ ($L$=CN, Cl, and Br) show the Giant Magnetoresistance (GMR) at low temperature owing to the strong intramolecular interaction between the local spin moment of Fe 3*d* electrons and $\pi$-electrons of Pc ring [42, 43, 44, 45]. Here, TPP denote tetraphenylphosphonium. Figure 4.2 shows the crystal structure of TPP[Fe(Pc)(CN)$_2$]$_2$. For the realization of the electron conduction, the HOMO of the Fe(Pc)(CN)$_2$ is considered to be partially oxidized, and the nominal charge of Pc ring is -1.5. The TPP[Fe(Pc)(CN)$_2$]$_2$ undergoes the insulating state at low temperature, where the GMR effect is observed [46, 47]. In order to understand this GMR effect, it is essential to clarify the electronic and geometric structure around molecular centered Fe depending on molecular arrangement or ligand. Therefore, we measured XANES spectra and performed multiple scattering calculations.

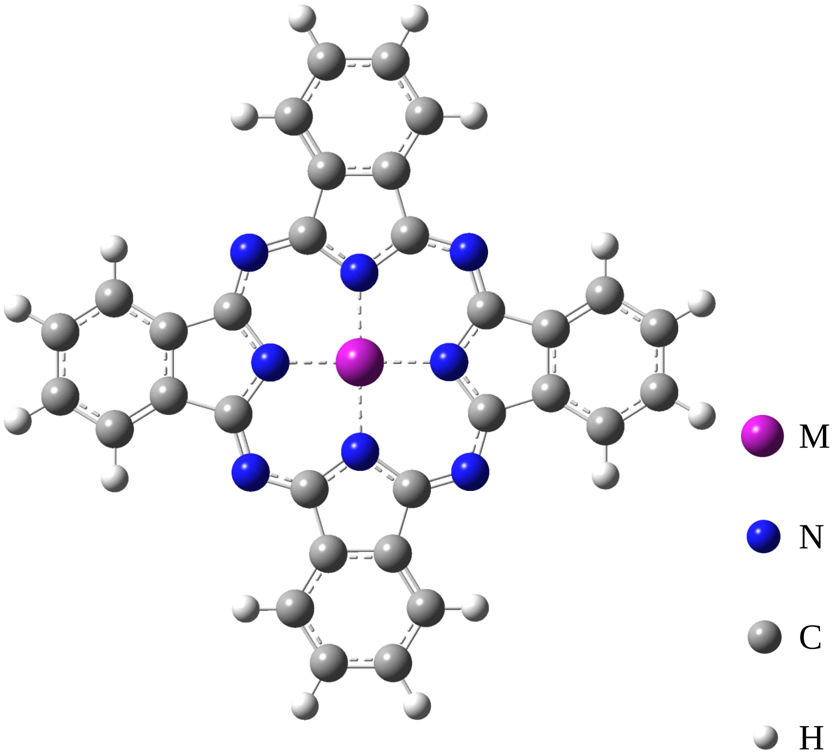

Figure 4.1: Chemical structure of Metal Pc molecule.

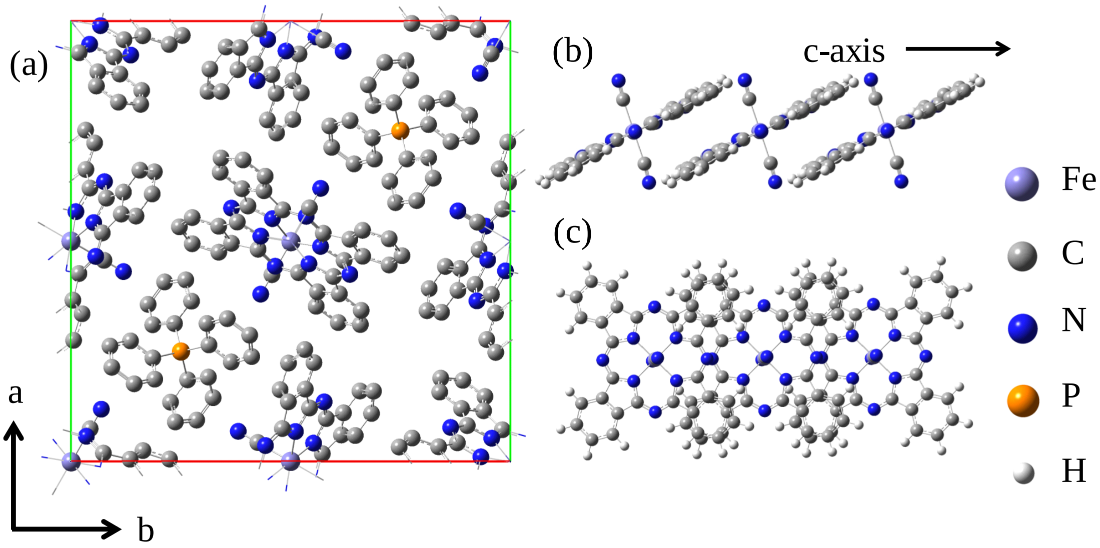

Figure 4.2: Crystal structure of TPP[Fe(Pc)$(CN)_2$]$_2$viewed from (a) the *c*-axis, and (b) perpendicular to the *c*-axis. (c) top view from the *c*-axis.

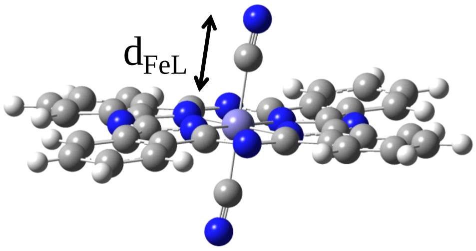

Figure 4.3: Distance between molecular centered Fe and ligand.

## 4.2 Experimental

The Fe K-edge X-ray absorption spectra in TPP[Fe(Pc)$(CN)_2$]$_2$, DMDP[Fe(Pc)$(CN)_2$], and [(n-$C_7H_{15}$)$_4$N][Fe(Pc)$(CN)_2$] were measured in the energy range from 7.1 to 7.2 keV at BL-14B1 in SPring-8. The sample disks are prepared by pressing the mixture of the BN and the sample powder. The X-ray absorption coefficient of the samples is obtained by measuring the intensity of the incident X-ray beam, that is passed through the double-crystal monochromator, and the transmitted beam by use of the ion chamber. To investigate the ligand effect, the Fe K-edge X-ray absorption measurements for TPP[Fe(Pc)$Br_2$]$_2$ and TPP[Fe(Pc)$(Cl)_2$]$_2$ were also performed at BL-39XU SPring-8 with the transmission method. The transmitted beam was measured by SSD detector.

For the TPP[Fe(Pc)$(CN)_2$]$_2$ system, the Fe K-edge X-ray absorption measurements are also performed at 12 K and 296 K under ambient pressure in order to investigate the structural change due to the temperature. Polarization dependence spectra whose x-ray polarization vector $E$ is parallel to $c$-axis and perpendicular to $c$-axis are also measured at 296 K.

## 4.3 Result and Discussion

### 4.3.1 Cation molecular dependence

In this section, ligand is fixed $L = CN$ however the cation is varied. The crystal information and distance between Fe and CN ligand are listed in table 4.1. The DMDP[Fe(Pc)$(CN)_2$] (DMDP=dimethyldiphenylphosphonium) and [(n-$C_7H_{15}$)$_4$N][Fe(Pc)$(CN)_2$] have the same Fe(Pc)$(CN)_2$ molecule as the TPP compound. In these two reference compounds, the Fe(Pc)$(CN)_2$ molecules are not oxidized, and the nominal charge of the Pc ring is -2. Thus these molecules do not show the GMR effect. The comparison with other compounds helps clarify the influence of the molecular structure and charge.

Figure 4.6 shows the experimental Fe K-edge XANES spectra for TPP[Fe(Pc)$(CN)_2$]$_2$, DMDP[Fe(Pc)$(CN)_2$] and [(n-$C_7H_{15}$)$_4$N][Fe(Pc)$(CN)_2$]. There is the difference in the spectra between three Fe(Pc)$(CN)_2$ compounds only in the energy region of 7134-7152 eV. The absorption in the TPP compounds, in which the nominal charge of Pc ring is -1.5, is higher than that in the DMDP and [(n-$C_7H_{15}$)$_4$N] compounds, in which the charge is -2. To investigate the origin of the spectral difference, we carried out the multiple scattering calculation. The calculation model were constructed by using the crystal structure data measured by Matsuda *et al* [44]. The electronic structure was calculated by Gaussian09 (B3LYP/LanL2DZ) [26]. In these three compounds, the molecular electronic structures such as the

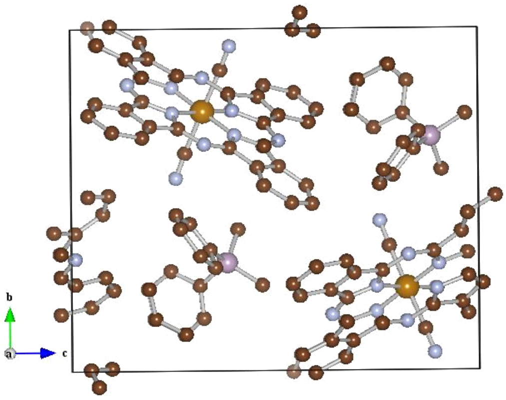

Figure 4.4: Crystal structure of DMDP[Fe(Pc)$(CN)_2$]$_2$ system.

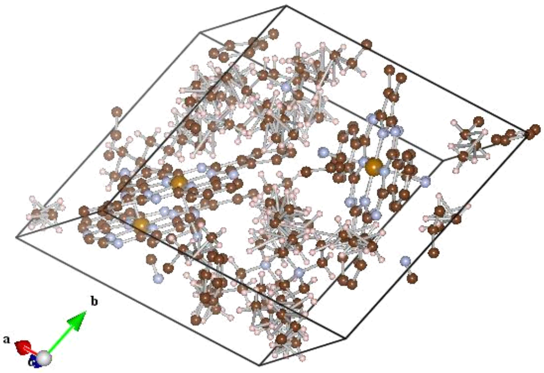

Figure 4.5: Crystal structure of [(n-$C_7H_{15}$)$_4$N][Fe(Pc)$(CN)_2$] system.

Table 4.1: Crystal structures of Fe(Pc)$(CN)_2$ systems.

| | TPP[Fe(Pc)$(CN)_2$]$_2$ | DMDP[Fe(Pc)$(CN)_2$] | [(n-$C_7H_{15})_4$N][Fe(Pc)$(CN)_2$] |
|---|---|---|---|
| Chemical formula | $C_{92}H_{52}N_{20}PFe_2$ | $C_{48}H_{32}N_{10}PFe$ | $C_{62}H_{60}N_{11}Fe$ |
| Formula weight | 1580.22 | 835.67 | 1015.08 |
| Crystal system | tetragonal | monoclinic | monoclinic |
| Space group | $P4_2$/n | Pc | Pc |
| $a$/Å | 21.407 | 8.5580 | 29.3500 |
| $b$/Å | 21.407 | 14.3117 | 15.40610 |
| $c$/Å | 7.386 | 17.3236 | 29.5700 |
| $\beta$/deg. | 90 | 99.848 | 25.2260 |
| $d_{FeL}$Å | 1.981 | 1.990 | 1.990 |

HOMO hardly differ from each other. The calculated XANES spectra are displayed in Fig.4.7. The overall feature of the XANES spectra and three peaks above the Fe K-edge are reproduced by the calculation. In the peak at $E-E_0 = 47$ eV, one can see the difference in the peak height between three compounds, which is consistent with the experimental result shown in Fig.4.6. In Fig.4.7(b), the peak height of DMDP[Fe(Pc)$(CN)_2$] and [(n-$C_7H_{15})_4$N][Fe(Pc)$(CN)_2$] in inverse for experimental shown in Fig.4.6(b). We think that the electronic state calculated by Gaussian could not represent accurate electronic state due to the ligand field effect, since the assumption of strong ligand field is not necessarily true in the real molecule.

Since the XANES spectra reflect the multi electron scatterings at atoms around the iron, it is important to examine the local structure around the iron atom. Figure 4.8 shows the molecular structure in three Fe(Pc)$(CN)_2$ compounds. The iron atom exists in the center of the four nearest-neighbor nitrogens in the Pc ring. The distance between the iron and the nitrogens is about 1.94 Å. This relation between the iron and the nearest-neighbor nitrogens holds in Fe(Pc)$(CN)_2$ compounds. The iron atom also has the coordination bond with the CN ligand. Table 4.1 lists the bond length between the Fe and C atom in the CN ligand. The angle between a Pc ring to CN ligands, and the angle of the iron to N and CN ligand are listed in table 4.2. In Table 4.2, $\theta$ and $\phi$ are defined as $\theta = \angle Pc - Fe - CN$ and $\phi = \angle Fe-C(CN)-N(CN)$, respectively. In [(n-$C_7H_{15})_4$N][Fe(Pc)$(CN)_2$], the avaraged Fe-C bond length is shown.

Owing to contact between the CN ligand and other molecules in the crystal, the CN ligand seems to be tilted from the direction perpendicular to the plane of the Pc ring, in which $\theta$ and $\phi$ are 90 and 180 (deg.), respectively. There is small difference in the bond length of Fe-C between the Pc compounds, as well. The difference of the XANES spectra in 7314-7152 eV is ascribable to the angle of the CN ligand,

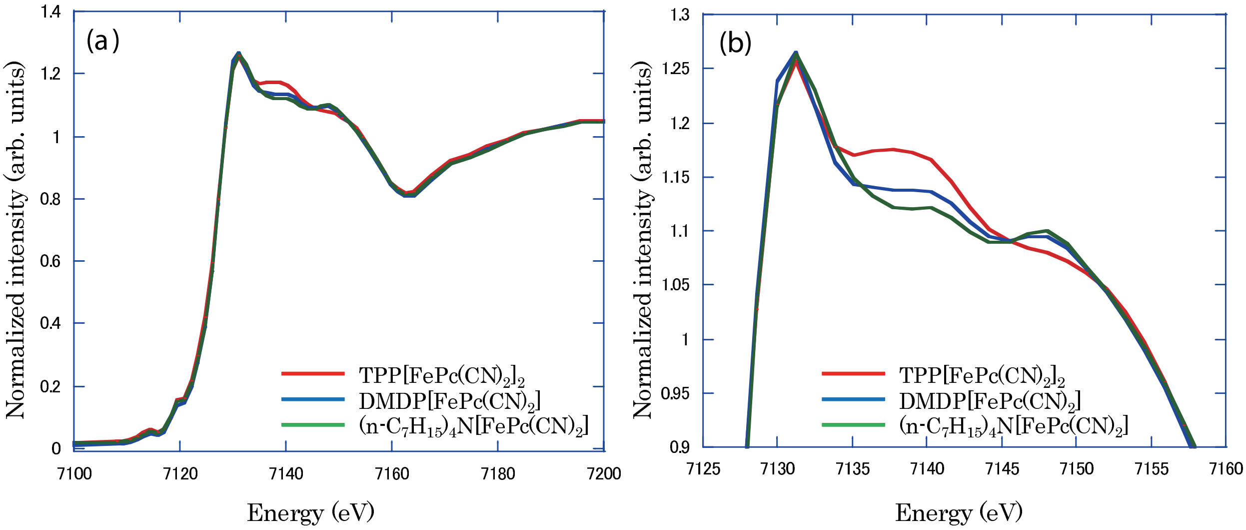

Figure 4.6: Observed Fe K-edge XANES spectra in the wide energy range (a) and above the absorption edge (b) for TPP[Fe(Pc)(CN)$_2$]$_2$(red), DMDP[Fe(Pc)(CN)$_2$](blue), and [(n-$C_7H_{15}$)$_4$N][Fe(Pc)(CN)$_2$](green).

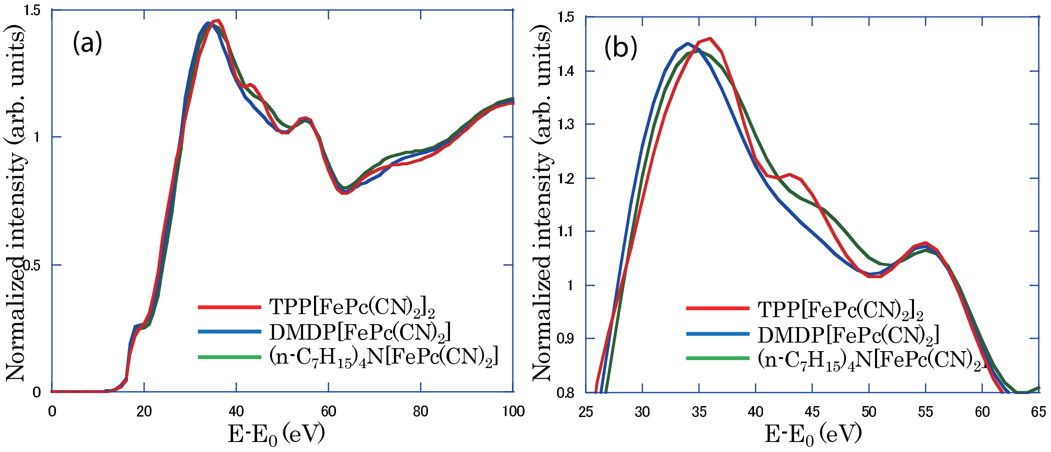

Figure 4.7: Calculated Fe K-edge XANES spectra in the energy range between $E - E_0 = 0 - 100$ eV (a) and 25-65 eV (b) for TPP[Fe(Pc)(CN)$_2$]$_2$(red), DMDP[Fe(Pc)(CN)$_2$](blue), and [(n-$C_7H_{15}$)$_4$N][Fe(Pc)(CN)$_2$](green). $E_0$ means the energy at the absorption edge.

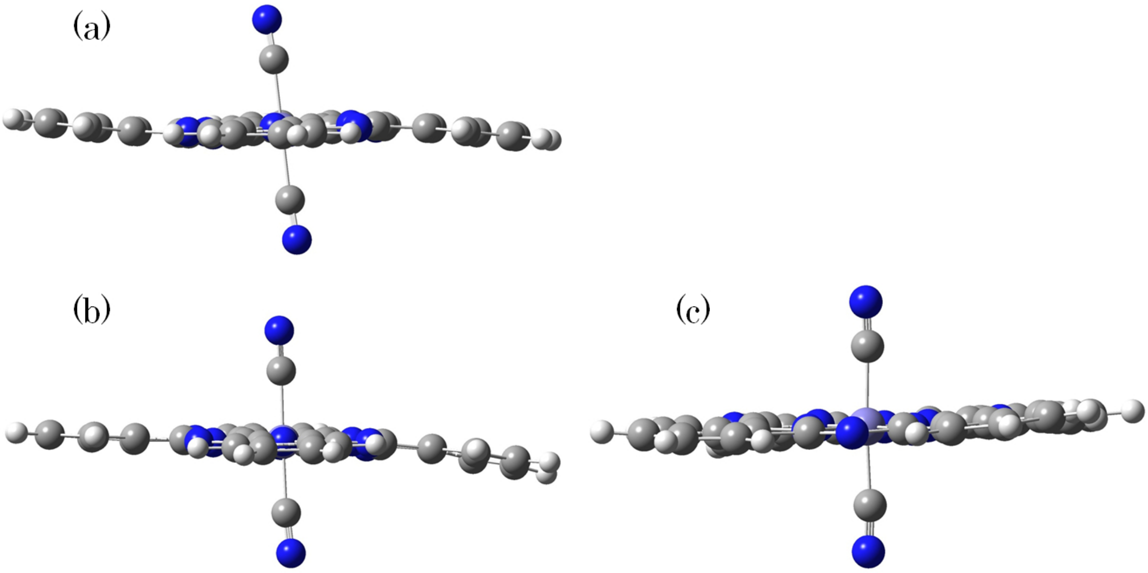

Figure 4.8: Molecular structure of TPP[Fe(Pc)(CN)$_2$]$_2$ (a), Molecular structure of DMDP[Fe(Pc)(CN)$_2$] (b), and Molecular structure of [(n-$C_7H_{15}$)$_4$N][Fe(Pc)(CN)$_2$] (c).

Table 4.2: Structure of the Fe atom and CN ligand in Fe(Pc)(CN)$_2$.

| Compounds | $\theta$ (deg.) | $\phi$ (deg.) |
|---|---|---|
| TPP[Fe(Pc)(CN)$_2$]$_2$ | 99.07 | 174.94 |
| DMDP[Fe(Pc)(CN)$_2$] | 96.41 | 175.25 |
| (n-$C_7H_{15}$)$_4$N[Fe(Pc)(CN)$_2$] | 91.56 | 175.36 |

the Fe-C bond length and Pc ring distortion. According to the structural study in other Fe(Pc)(CN)$_2$ compounds, the Fe-C bond length seems to change with the nominal charge of the Pc molecules. The spectra in this energy range can be considered as an indicator of the Pc molecular charge in Fe(Pc)(CN)$_2$.

### 4.3.2 Ligand dependence

Through the GMR effect is also observed in the Br and Cl compounds, the intensity of the GMR effect obeys the ligand strength called spectrochemical series [45]. In order to investigate the axial ligand effect on the XANES spectra, we changed the CN ligand into Br and Cl however cation molecule is fixed to TPP. Table 4.3 shows the crystal information of TPP[Fe(Pc)$L_2$]$_2$ systems. The distances between central Fe and the axial ligand are also listed in table 4.3.

Table 4.3: Crystal structures of TPP[Fe(Pc)$L_2$]$_2$ systems

| | TPP[Fe(Pc)(CN)$_2$]$_2$ | | TPP[Fe(Pc)Cl$_2$]$_2$ | TPP[Fe(Pc)Br$_2$]$_2$ |
|---|---|---|---|---|
| Temperature (K) | 30 | 293 | 123 | 123 |
| Chemical formula | $C_{92}H_{52}N_{20}PFe_2$ | | $C_{88}H_{52}N_{16}Fe_2Br_4P$ | $C_{88}H_{52}N_{16}Cl_4Fe_2P$ |
| Crystal system | tetragonal | | tetragonal | tetragonal |
| Space group | $P4_2$/n | | $P4_2$/n | $P4_2$/n |
| $a = b$/Å | 21.407 | 21.722 | 21.49 | 21.410 |
| $c$/Å | 7.386 | 7.448 | 7.472 | 7.5777 |
| $d_{FeL}$Å | 1.967 | 1.981 | 2.304 | 2.431 |

Table 4.4: The number of Fe 3$d$ electrons of TPP[Fe(Pc)$L_2$]$_2$ system obtained by LDA calculation

| | TPP[Fe(Pc)(CN)$_2$]$_2$ | | TPP[Fe(Pc)Cl$_2$]$_2$ | TPP[Fe(Pc)Br$_2$]$_2$ |
|---|---|---|---|---|
| Temperature (K) | 30 | 293 | 123 | 123 |
| Number of Fe 3$d$ electrons | 6.724 | 6.797 | 6.774 | 6.799 |

We take into account not only central Fe(Pc)$L_2$ molecule but also the neighboring Fe(Pc)$L_2$ and TPP molecules within the region whose radius from the central Fe atom is 10 Å, since the atoms within ~ 8 Å from the X-ray absorbing atom affect the XANES spectra. Figures 4.9 (a) and (b) display the experimental and calculated result in TPP[Fe(Pc)$L_2$]$_2$ ($L$=CN, Br, and Cl), respectively. The overall feature of our multiple scattering calculation has the similar incident-energy dependence to the experimental results. Here we apply local density approximation (LDA) calculation to the cluster models which are constructed by the crystal structures in order to obtain the electronic structure. The cluster model includes 369 atoms for $L$=CN and 363 atoms for $L$=Cl, Br. Table 4.4 lists the number of the 3$d$ electrons in the central iron obtained by the LDA calculations. The electronic structure hardly depends on the ligands $L$.

In the case of $L$=CN, the absorption edge shifts toward higher energy about 3 eV compared with $L$=Br and Cl. The difference in the absorption edge energy between Fe(II) and Fe(III) is expected to be about 5 eV [48, 49]. Therefore, the edge shift is ascribed to the intensity of the hybridization of Fe 3$d$ and the ligand $p$ orbital, and the distance between Fe and the axial ligand. The pre-edge peaks around 7112 eV are observed in the all cases. In the case of $L$=CN, the additional pre-edge peak is also observed around 7118 eV. If these two pre-edge peaks reflect the quadrupole transition, the energy splitting should be usually about 2 ~ 3 eV [50, 51]. Thus, the second peak is considered to be some other effect like metal-metal interaction [52].

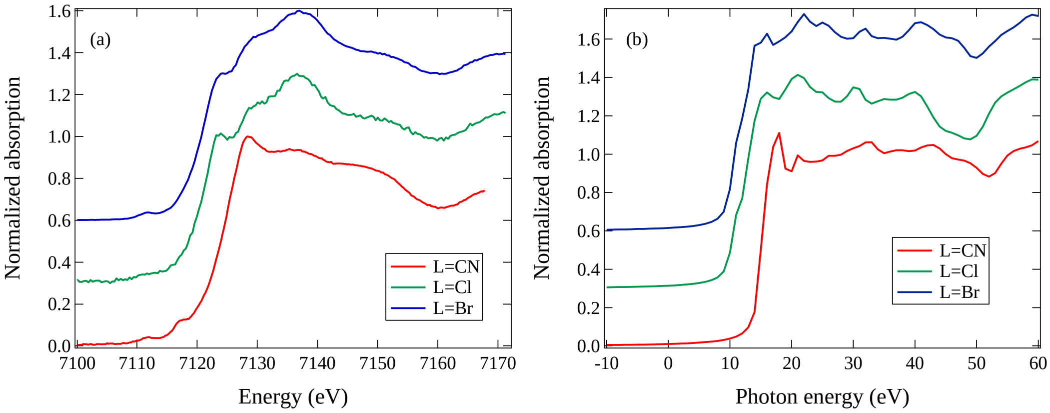

Figure 4.9: (a)Experimental Fe K-edge XANES spectra with changing ligand at TPP[Fe(Pc)$L_2$]$_2$ molecules($L$=CN, Br, Cl). (b)Calculated Fe K-edge XANES spectra reflected with changing the ligand.

### 4.3.3 Temperature and polarization dependence

In this section, we only focus on the TPP[Fe(Pc)(CN)$_2$]$_2$ molecule in order to investigate the effect of the structural change and the contribution of molecular orbital to the absorption edge. In this molecule, the structural change is seen near the temperature which shows anomaly of magnetic susceptibility. The inflection of the resistivity is observed as well [45].

Figure 4.10 shows the temperature dependence in the Fe K-edge XANES spectra of TPP[Fe(Pc)(CN)$_2$]$_2$. The experimental result suggests that there is the difference in the spectral height near the absorption edge between 296 K and 12 K. The electronic structure is calculated by LDA for the cluster model whose radius is 10 Å made by crystal structure at 293 K and 30 K [44]. As listed in Table 4.4, there is no significant change of the number of electrons. Therefore, the change of spectral shape is also caused by the variation of the distance between central Fe and axial ligand of CN.

In order to investigate the character of the orbital contributing to the absorption edge, we investigate the polarization dependence. Figure 4.11 (a) shows the experimental result of the Fe K-edge XANES spectra for $L$=CN for the polarization direction parallel and perpendicular to the $a$-axis and $c$-axis. We also show the calculated spectra for the polarization direction parallel to the $a$-axis and $c$-axis in Fig. 4.11 (b). The difference in the height for the polarization direction is seen just above the absorption edge. The spectral height for polarization direction parallel to the $c$-axis is smaller than that for the direction perpendicular to the $c$-axis. Since the electron is excised to the molecular orbital having the character of Fe 4$p$ orbital

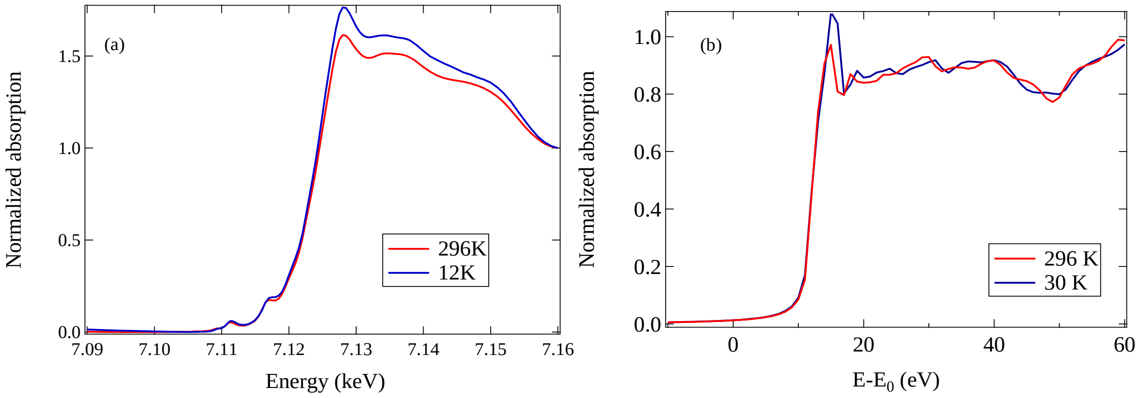

Figure 4.10: Temperature dependence of (a) experimental and (b) calculated Fe K-edge XANES spectra of TPP[Fe(Pc)$(CN)_2$]$_2$ system.

near the Fe K-edge, one possible origin of the spectral differences is the character of molecular orbital near the absorption edge. The molecular orbital calculation for TPP[Co(Pc)$(CN)_2$]$_2$ that is isostructural compound of TPP[Fe(Pc)$(CN)_2$]$_2$, indicates that the molecular orbital having large component of $4p_z$ orbital has lower energy than the molecular orbital having the large component of $4p_x$ and $4p_y$ orbital. Here, z direction is defined as the direction nearly parallel to the ligand direction, while the x and y directions are parallel to the Pc molecular plane. For the polarization along the $z$ direction (the CN ligand direction), the height of the XANES just above the K-edge is expected to be higher than that for polarization along the $x$ and $y$ direction (the Pc molecular plane). As shown in Fig. 4.2 (c), Fe(Pc)$(CN)_2$ molecules stack along the *c*-axis. The CN ligand direction is close to the *ab* plane rather than the *c*-axis. Thus, the height of the XANES for $E$ // the *ab* plane is also anticipated to be higher than that for $E$ // the *c*-axis. This discussion is consistent with the experimental result of Fig. 4.11 (a) and the calculated result of Fig. 4.11 (b).

## 4.4 Conclusion

We reported the XANES spectra in the (phthalocyaninate)iron compounds. In the case of cation molecular dependence, the Fe K-edge XANES spectra show the difference in the region 7134-7152 eV. To analyze that difference, we performed the multiple scattering calculations, and revealed that the spectral difference is ascribable to the difference of the Fe(Pc)$(CN)_2$ molecular structure, that changes with the Pc molecular charge and stacking.

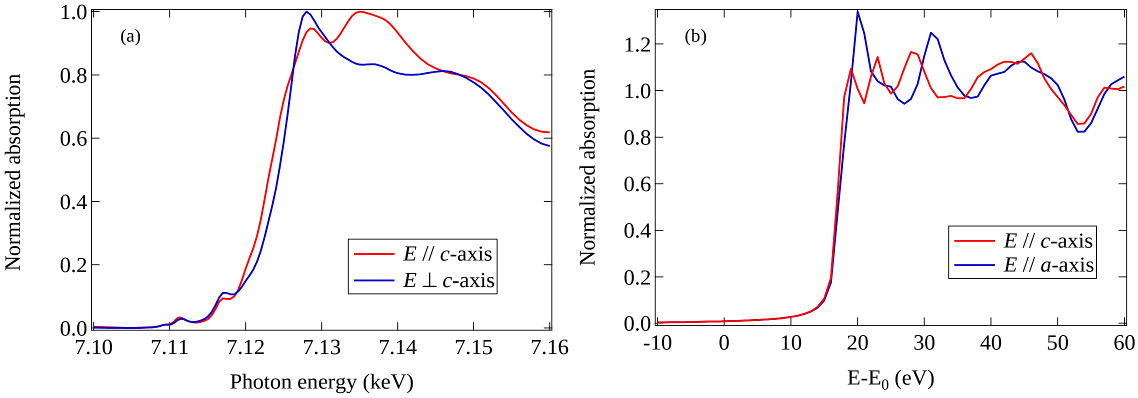

Figure 4.11: Polarization dependence of (a) experimental and (b) calculated Fe K-edge XANES spectra of TPP[Fe(Pc)$(CN)_2$]$_2$ system. *E* means X-ray polarization vector.

For the TPP[Fe(Pc)$L_2$]$_2$ ($L$=CN, Cl and Br) system, we investigate the Fe K-edge XANES spectra to analyze the ligand effect. The number of the Fe 3*d* electrons obtained by the LDA calculations hardly depends on the ligand. The experimental Fe K-edge XANES spectra show the energy shift of the absorption edge. This shift is explained by the magnitude of the d-p hybridization called the specrochemical series. Our multiple scattering calculations suggest that the spectral shape is strongly influenced by the distance between the central Fe and the axial ligands $L$. The temperature variation of the intensity in absorption edge is observed and is also explained by the change of the Fe-CN distance. The polarization dependence spectra on the absorption edge may be explained by the character of the molecular orbital. If the molecular orbital existing just above the absorption edge has the large component of the 4*p* orbital, the height of the XANES is anticipated to increase for the polarization direction parallel to the direction, in which 4*p* orbital is elongating. Our multiple scattering calculations are consistent with the experimental results.

# Chapter 5

# Local structure of iodine-doped polyvinyl alcohol (PVA) film studied by iodine K-edge XAFS spectra

## 5.1 Iodine-doped PVA film

The films of iodine-doped polyvinyl alcohol (I-PVA) have been applied to high quality polarizer because their photoabsorption in ultraviolet and visible region is highly anisotropic for stretched film [53, 54, 55, 56, 57]. The absorption wave length and the polarization dependence are sensitive to the concentration of polyiodide $I_3^-$ and $I_5^-$ anions and to the orientation of the molecular axis of polyiodide species in PVA films. Yokoyama *et al.* have applied iodine K-edge extended X-ray absorption fine structure (EXAFS) analysis to I-PVA films, and they have shown that the molecular axes of the polyiodine species are nearly parallel to the PVA chain based on polarization dependent EXAFS [58]. Miki *et al.* have reported the iodine K-edge polarization dependent X-ray absorption near edge structure (XANES) spectra for $I_5^-$-PVA [59]. The remarkable polarization dependence has been observed around 33160 eV. They have reported that the molecular orbital calculations have shown that only 5$p$ orbital parallel to the polyanion axis have vacancies. It implies that the strongest X-ray absorption intensity for the linear polarization may be parallel to the polyanion axis.

There still remain several controversies concerning the local structure of I-PVA films. In this section, we report the I K-edge EXAFS analysis for $I_3^-$-PVA film and $I_5^-$-PVA film and XANES analysis for $I_3^-$-PVA film.

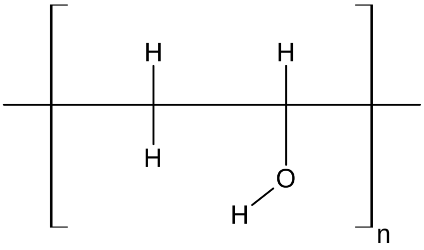

Figure 5.1: Molecular structure of PVA.

## 5.2 Experimental

The I-PVA films which were produced by Kuraray Co. Ltd., Japan were stretched in boric acid solution. The degrees of polymerization and saponification were 2400 and greater than 99 %, respectively. I K-edge XAFS spectra were measured for I-PVA films in the transmission mode at the BL-08, SPring-8 in Japan at room temperature in atmospheric pressure. The angle $\theta$ between X-ray polarization vector and the film stretching direction is varied as 0°, 45° and 90° which is shown in Fig. 5.2 in order to investigate polarization dependence.

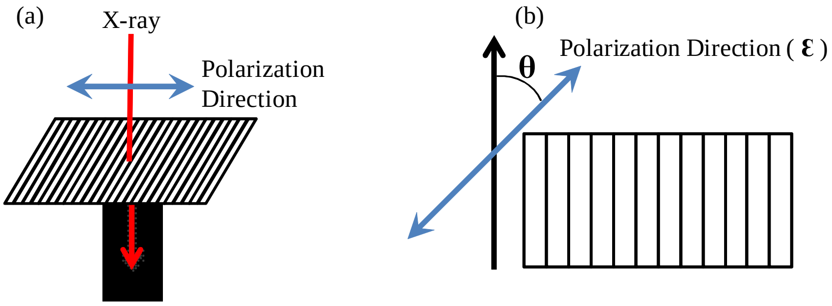

Figure 5.2: Schematic picture of (a) X-ray incident direction and (b) the direction of extension of I-PVA film.

## 5.3 Result and discussion

### 5.3.1 EXAFS analysis

Figure 5.3 shows the experimental iodine K-edge EXAFS spectra in k-space. The region of $k = 4 \sim 14\text{Å}^{-1}$ is mainly contributed by I-I scattering. The magnitude of the EXAFS oscillation is decrease with varying the angle. The oscillation phase of $\theta = 90°$ is different from the case of $\theta = 0°$ and $\theta = 45°$ especially low k region. It implies that the oscillation shows the scattering from oxygen or carbon atoms on PVA chain. We shall analyze this region as XANES in order to investigate the relation between the iodine and PVA chain.

Figure 5.4 shows the Fourier transformed experimental iodine K-edge EXAFS spectra of $I_3^-$-PVA film and $I_5^-$-PVA film with varying X-ray polarization angle $\theta = 0°$, 45° and 90°. The experimental spectrum of the case of $\theta = 0°$ shows the information for the stretching direction of the film. Therefore the peak around 2.7 Å for $I_3^-$-PVA film and 2.5 Å for $I_5^-$-PVA film shows the distance between iodide atom in PVA film and the peaks around 2.0 Å are due to strong k dependence of the backscattering amplitude of iodine. The single scattering EXAFS formula for oriented samples is described as follows

$$\chi(k) = S_0^2 N^*(\Theta) \frac{|F(k)|}{kR^2} e^{-2\sigma^2 k^2} e^{\frac{-2R}{\lambda}} \sin(2kR + \psi(k)) \tag{5.1}$$

here $N^*(\Theta)$ is effective coordination number and $\Theta$ means the angle between X-ray polarization vector and the direction of film expansion. The Fourier transformed EXAFS spectra are fitted by equation (5.1) using ATHENA and ARTEMIS [30, 31, 60] and obtained parameters are listed in table 5.1. In the case of $I_3$-PVA, the fit is performed by single shell. The case of $I_5$-PVA, the fit is performed by two shells because $I_5$-PVA has two different I-I distance and the fit is failed by single shell. As a result of curve fitting of EXAFS spectrum for $\theta = 0°$, the distance between iodide anions in PVA film is 2.92 and 2.79 Å for $I_5^-$-PVA film and 2.92 Å for $I_3^-$-PVA film. Sakane *et al.* has reported the distance between iodine in triiodide anion in several solvents [61]. According to their result, the distance between iodine is 2.91 ~ 2.92 Å. This result implies that the condition of triiodide anion in PVA film is similar to the condition in several organic solvent.

Figure 5.5 shows the amplitude parameter $S_0^2 N^*$ obtained by fitting. When sample has perfect orientation, $N^*$ is described as

$$N^* = 3N \cos^2 \Theta \tag{5.2}$$

here $\Theta$ means the angle between the electric field vector of X-ray and the polyiodide molecular axis. The obtained parameters do not obey the equation (5.2). It implies that the polyiodide has angular distribution. In order to analyze the angular dependence of the amplitude parameter obtained by fitting, we assume that the angular distribution of polyiodide molecular axis $\hat{\boldsymbol{l}}(\theta, \phi)$ to be Gaussian distribution. Where $\theta$ is the angle between $\hat{\boldsymbol{l}}$ and film stretch direction. The distribution function $\rho$ is described as follows.

$$\rho(\theta, \phi) d\Omega = \frac{1}{\sqrt{2\pi^3\Delta^2}} \exp^{-\frac{\theta^2}{2\Delta^2}} d\theta d\phi \tag{5.3}$$

where $\Delta$ means standard variation. Here we assume that the film stretch direction is parallel to the $z$-axis and the distribution of the molecular axis for $\phi$ direction is uniform. From these assumption, the effective coordination number is described by the following equation,

$$N^* = N \langle \cos^2 \gamma \rangle \tag{5.4}$$

here $N = \frac{4}{3}$ for $I_3^-$-PVA, $N = \frac{4}{5}$ for each shell for $I_5^-$-PVA and $\langle \cos^2 \gamma \rangle$ is given by

$$\int \cos^2 \gamma \cdot \rho d\Omega = \frac{1}{4}(1 + \exp^{-2\sigma^2})(2 \cos^2 \Theta - \sin^2 \Theta) + \frac{1}{2} \sin^2 \Theta \tag{5.5}$$

where $\cos \gamma$ means the angle between electric field vector of X-ray $\hat{\boldsymbol{E}}$ and unit vector of $\hat{\boldsymbol{l}}$. EXAFS amplitude is too small in the case of $I_3^-$-PVA. There is some component which does not contribute to I-I EXAFS amplitude. One of the reason may be excess amount of $I^-$ when the sample synthesis. When we perform fitting of the EXAFS amplitude by using the equation (5.5), we include the additional parameter $\alpha$ which means the ratio of no contribution to the EXAFS amplitude factor like $I^-$ species. The fitting model for Fourier transformed EXAFS spectra is only included I-I scattering path and the distance between iodine is 2.9 Å. Figure 5.5 shows the fitting result and we obtain $\Delta$ and $\alpha$ from fitting result which is listed in 5.2.

| | $I_5^-$-PVA | | | $I_3^-$-PVA | | |
|---|---|---|---|---|---|---|
| angle (deg.) | 0 | 45 | 90 | 0 | 45 | 90 |
| $S_0^2 N^*$ | 0.5152 | 0.2380 | 0.009 | 0.1148 | 0.0605 | 0.008 |
| $r$ (Å) | 2.9254050, 2.78836 | | | 2.9201290 | | |
| $\sigma^2$ | 0.0055000, 0.0098210 | | | 0.0090110 | | |
| $\delta$ $E_0$ | 2.5916080 | | | 9.7939810 | | |

Table 5.1: The result of EXAFS fitting of $I_5^-$-PVA and $I_3^-$-PVA films.

### 5.3.2 XANES analysis

Figure 5.6 shows the I K-edge XANES spectra for the $I_3^-$-PVA and $I_5^-$-PVA films with different polarizations. There is strong polarization dependence around 33160

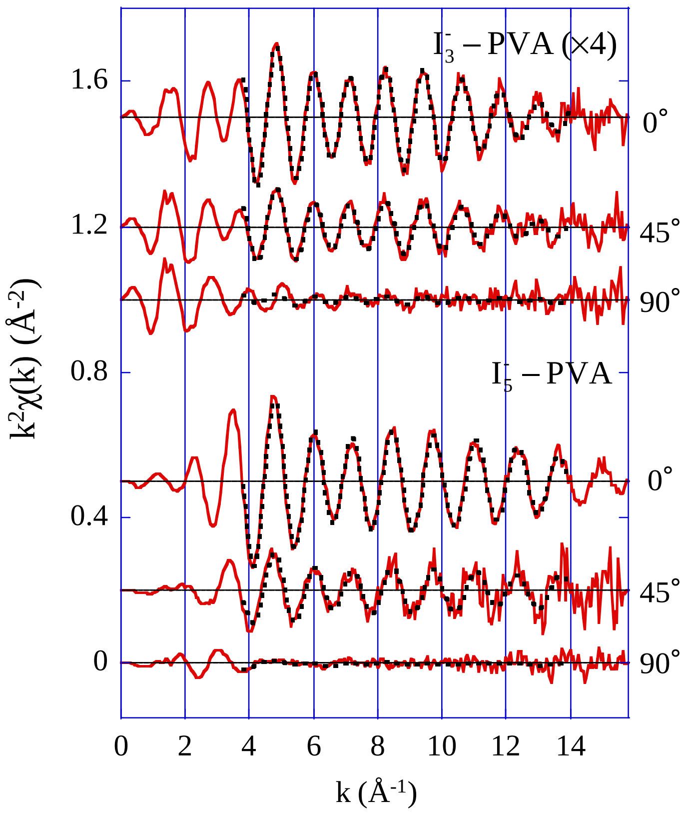

Figure 5.3: Polarization dependence of iodine K-edge EXAFS spectra $k^2\chi(k)$ for $I_3^-$-PVA and $I_5^-$-PVA films. Spectra of $I_3^-$-PVA film are multiplied by a factor of 4. Curve fitting results are also shown in dashed lines.

eV especially for the case of $I_5^-$-PVA. Molecular orbital calculation performed by Gaussian [26] shows that polyiodide anion in $I_5^-$-PVA have large amount of vacancies of 5$p$ orbital compared with its in $I_3^-$-PVA. Therefore the polarization dependence is ascribed to the vacancies of $\sigma^*$ orbital which is composed of 5$p_z$ and other molecular orbitals which are consisted to be fully occupied 5$p_x$ and 5$p_y$.

From the I K-edge EXAFS analysis for I-PVA film, we can obtain the information about the distance between iodide anion inside PVA film. Here we discuss the distance between iodide anion and PVA chains and the number of surrounding PVA chains from I K-edge XANES spectra. In order to investigate the XANES spectra, we construct structural models for $I_3^-$-PVA film. Figure 5.7 shows the structural model for the XANES calculation, whose I-I distance in the polyiodide anion which is obtained by EXAFS analysis is fixed at 2.92 Å, and the distance between the polyiodide anion and four PVA chains range from 5.25 to 5.40 Å. The

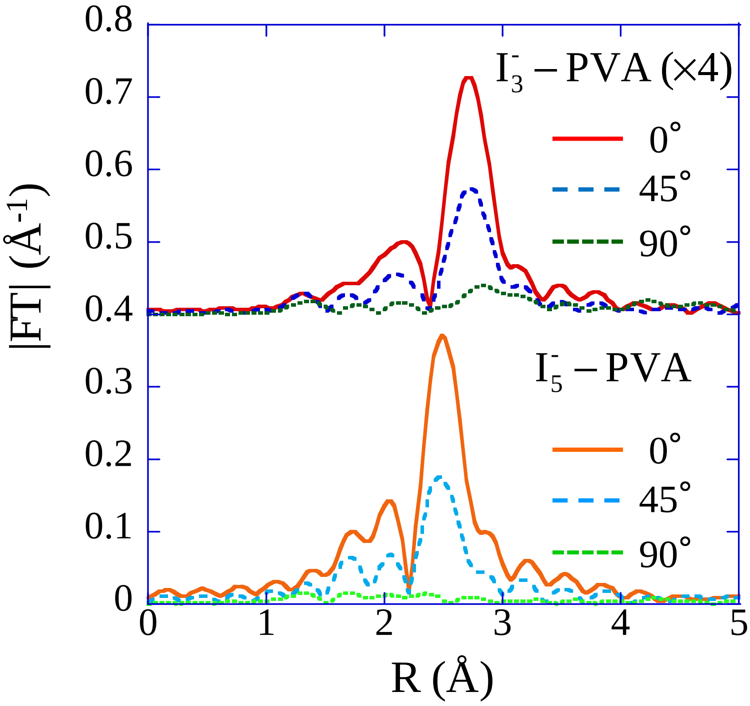

Figure 5.4: Polarization dependence of Fourier transformed iodine K-edge EXAFS spectra $k^2\chi(k)$ for $I_3^-$-PVA and $I_5^-$-PVA films. Spectra of $I_3^-$-PVA film are multiplied by a factor of 4. The angle between film stretch direction and x-ray polarization vector is given in figure.

model structure is optimized by using Gaussian (B3LYP/LanL2DZ) [26]. The energy region from 33210 to 33250 eV can be consider to contain information about the local structure around polyiodide due to the multiple scattering effect, we investigate this region by use of derivative spectra. Figure 5.8 shows the comparison between calculated I K-edge derivative XANES spectra with varying the distance between polyiodide and PVA chains and the experimental result. The oscillation obtained by calculation shows good agreement with experimental one when the distance between polyiodide and PVA chains are 5.35 Å. Figure 5.9 shows the calculated I K-edge derivative XANES spectra obtained by another model whose polyiodide is surrounded by six PVA chains. This model have been also optimized by Gaussian (B3LYP/LanL2DZ). Any calculated results do not corresponding to the experimental one.

These result suggests that the polyiodide anion is surrounded by four PVA chains, and the distance between polyiodide anion and PVA chain is 5.35 Å.

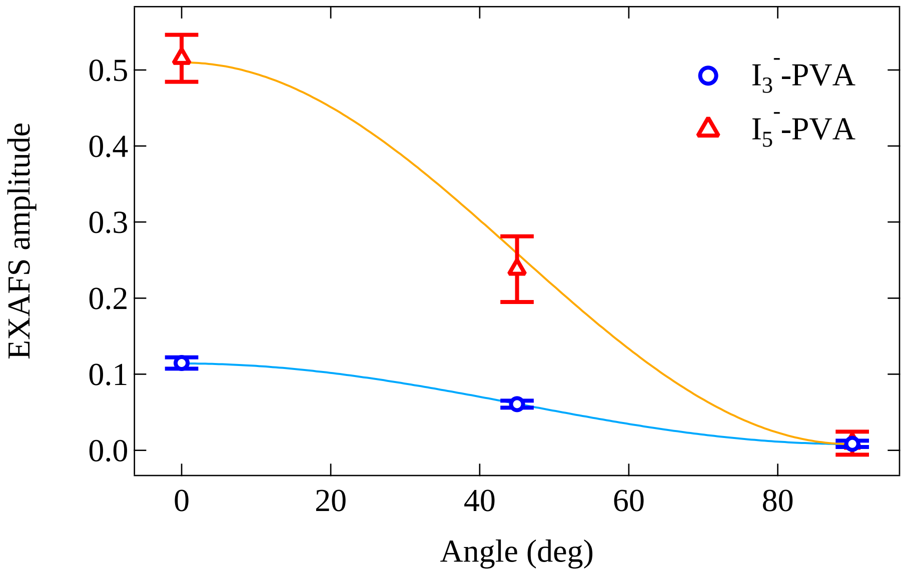

Figure 5.5: Polarization dependence of the nearest I-I amplitude parameter obtained from EXAFS curve fitting analysis for $I_3^-$-PVA and $I_5^-$-PVA samples. Solid curves are model fitting which include finite angular distribution of the polyiodide molecular axis (see text).

| | $I_5^-$-PVA | $I_3^-$-PVA |
|---|---|---|
| Δ (deg.) | 10.2±9.5 | 21.8±5.4 |
| $\alpha$ | 0.248±0.06 | 0.814±0.01 |

Table 5.2: The result of FT EXAFS amplitude for $I_5^-$-PVA and $I_3^-$-PVA film.

## 5.4 Conclusion

In this section, we study the polarization dependence of iodine K-edge XAFS spectra in order to investigate the local structure around iodide anion. From EXAFS analysis, we obtain the distance between polyiodide anion and the angular distribution of polyiodide anion inside PVA chain. In the case of $I_5^-$-PVA film, the distances between iodide anions are 2.92 and 2.79 Å. The angular distribution of polyiodide inside PVA chain is estimated as 10.2 ± 9.5 ° by EXAFS analysis. In the case of $I_3^-$-PVA film, the distance between iodide anions is 2.92 Å. The angular distribution of polyiodide inside PVA chain is estimated as 21.8 ± 5.4 ° by EXAFS analysis. From XANES analysis, we obtain the number of surrounding PVA chains and the distance between polyiodide and PVA chains. In the case of $I_3^-$-

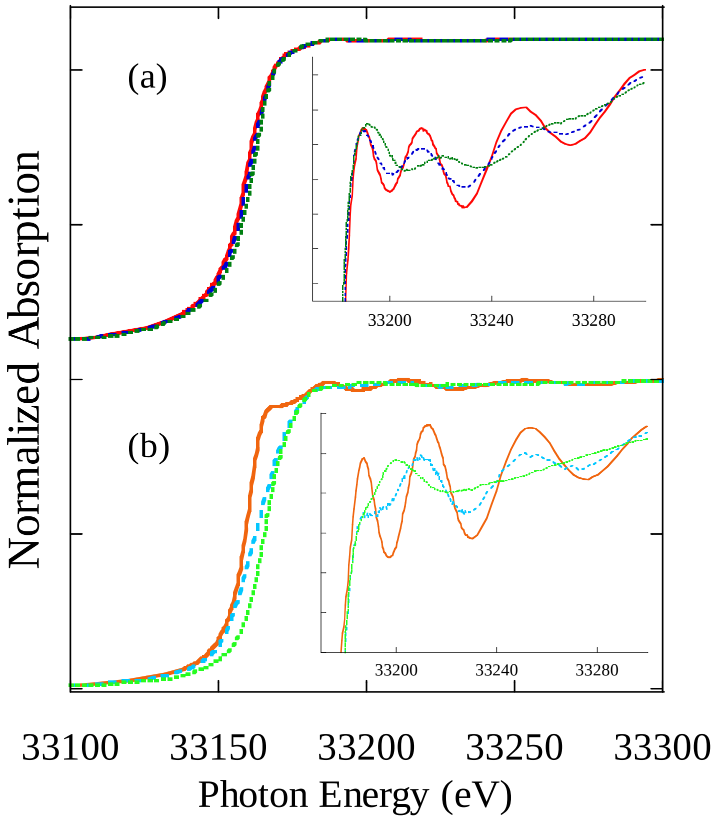

Figure 5.6: Polarization dependence of the iodine K-edge XANES spectra of (a) $I_3^-$-PVA and (b) $I_5^-$-PVA samples. Insets show enlarged near edge region.

PVA film, the calculated iodide K-edge derivative XANES spectra suggests that the polyiodide anion is surrounded by four PVA chains and the distance between the polyiodide and PVA chain is 5.35 Å.

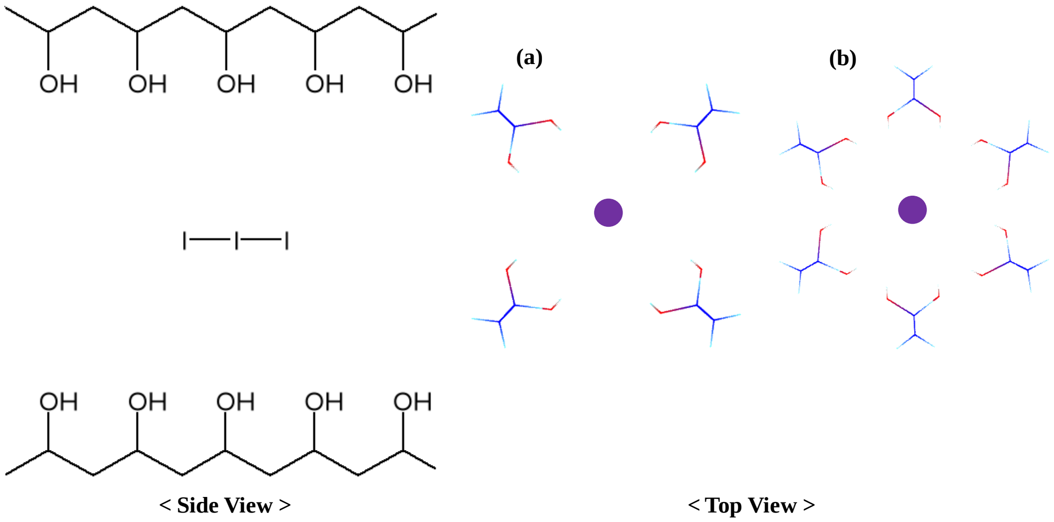

Figure 5.7: Structural models of $I_3^-$-PVA for the XANES calculations. I-I distances in polyanion $I_3^-$ are fixed at 2.92 Å as determined by the EXAFS analyses. (a): In model 1, the polyanion $I_3^-$ is surrounded by four PVA chains whose hydroxyl groups are oriented to the polyanion. (b): In model 2, the polyanion $I_3^-$ is surrounded by six PVA chains instead of four.

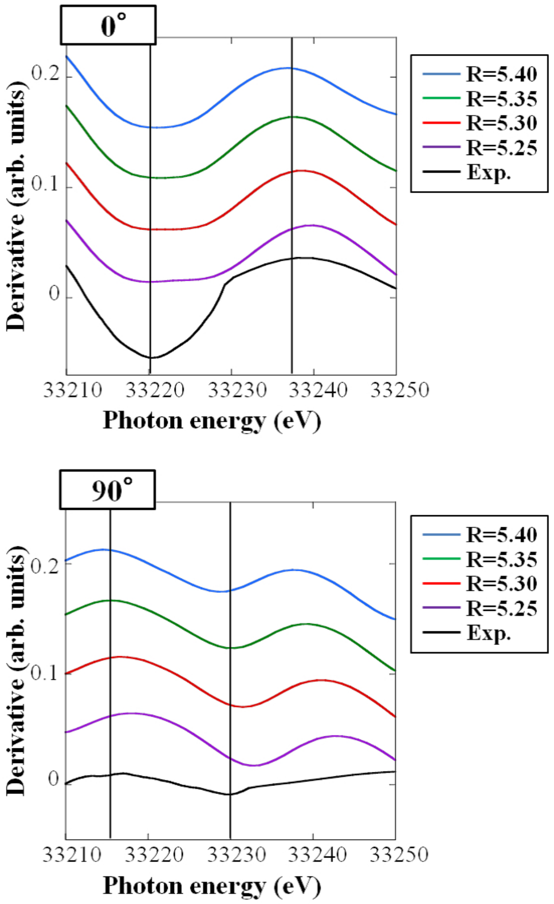

Figure 5.8: Iodine K-edge XANES derivative spectra from the results of the multiple scattering calculations obtained from four PVA chains model for varying I-C distance from 5.25 to 5.40 Å and the experimental results. The upper graph shows the case of $\theta = 0^\circ$ and the lower one shows the case of $\theta = 90^\circ$. The theoretical results are in good agreement with the experimental calculations in four PVA chain model when I-C distance is 5.35 Å.

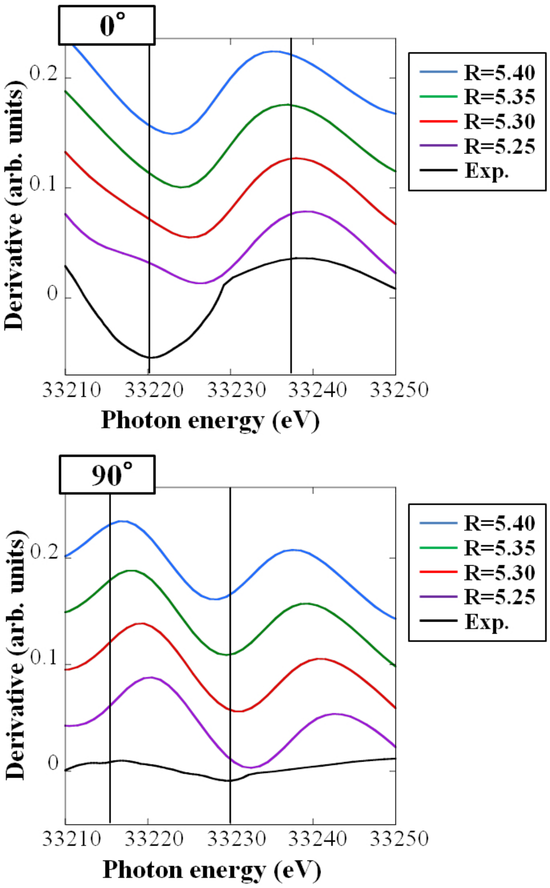

Figure 5.9: Iodine K-edge XANES derivative spectra from the results of the multiple scattering calculations for the another model whose polyiodide anion is surrounded by six PVA chains and the experimental results. The upper graph shows the case of $\theta = 0°$ and the lower one shows the case of $\theta = 90°$. The agreement is poor for the six PVA chain model for any I-C distance.

# Chapter 6

# Third row element K-edge XANES analysis for absorption edge anomaly

## 6.1 Introduction

The third row elements, Na, Mg, Al, Si, P, S, Cl, widely exist in the Earth. These elements are commonly used for industry and biological systems.

The K-edge absorption edge energies of these element are in soft X-ray energy region shown in Fig. 6.1 [10].

The K-edge XANES spectra are measured for many compounds including these light elements. The theoretical approaches to XANES spectral analysis can be classified into three groups: those based on the molecular orbital (MO) method, density functional theory (DFT) method, and multiple scattering method. In the case of multiple scattering method, the scattering process is described in reciprocal lattice space such as SPR-KKR [62] or in real space such as FEFF [30].

Although some of the theoretical analysis of K-edge XANES spectra are used screened core hole calculation [63], many of them are performed by using Z+1 approximation [64, 65, 66, 67]. The Z+1 approximation is a model for core electron excitation phenomena. If a deep core electron is excited from nucleus Z into an unoccupied valence orbital, the nucleus charge is reduced and the number of valence electron is increased by one. Therefore we can assume that the state of the system obtained the excited electron from the core orbital may be similar to the ground state of the system with X-ray absorbing atom Z+1 instead of the atom Z.

Figure 6.2 shows the experimental and calculated K-edge XANES spectra of simple substance of third row elements and some compounds [3]. Some of the

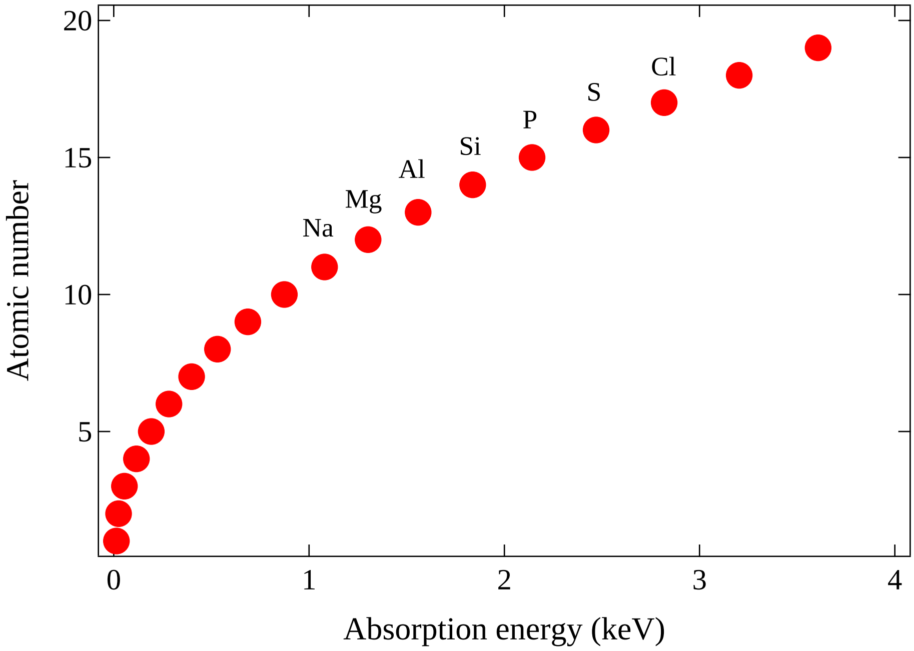

Figure 6.1: K-edge absorption edge energy for third row elements.

screened core hole calculations successfully reproduce the experimental XANES spectra. However, in most cases the calculation cannot explain the experimental spectra. According to D. Cabaret *et al.*, the reason is the vibrational effect because of the weight of these elements [68]. According to E. Tanuma *et al.*, the reason is the screening core hole process because these elements only have *s* and *p* electrons [66]. Although there are some reports refer to the reason, it has not been well understood why the screened core hole calculation does not work well. In this section, we study the K-edge XANES spectra of third row elements with applying full multiple scattering theory in order to investigate the reason why the screened core hole calculation does not work and effect of the Z+1 approximation.

## 6.2 Calculation

In order to investigate K-edge XANES spectra of these third row light elements, we apply multiple scattering theory. The calculation models are simple substrate whose radius are 8 Å were constructed by using crystal structure data [69, 70]. Here we apply local density approximation (LDA) calculation to the cluster models in order to obtain the electronic structure. We apply Muffin-tin approximation in which the potential is assumed to be spherically symmetric inside muffin-tin

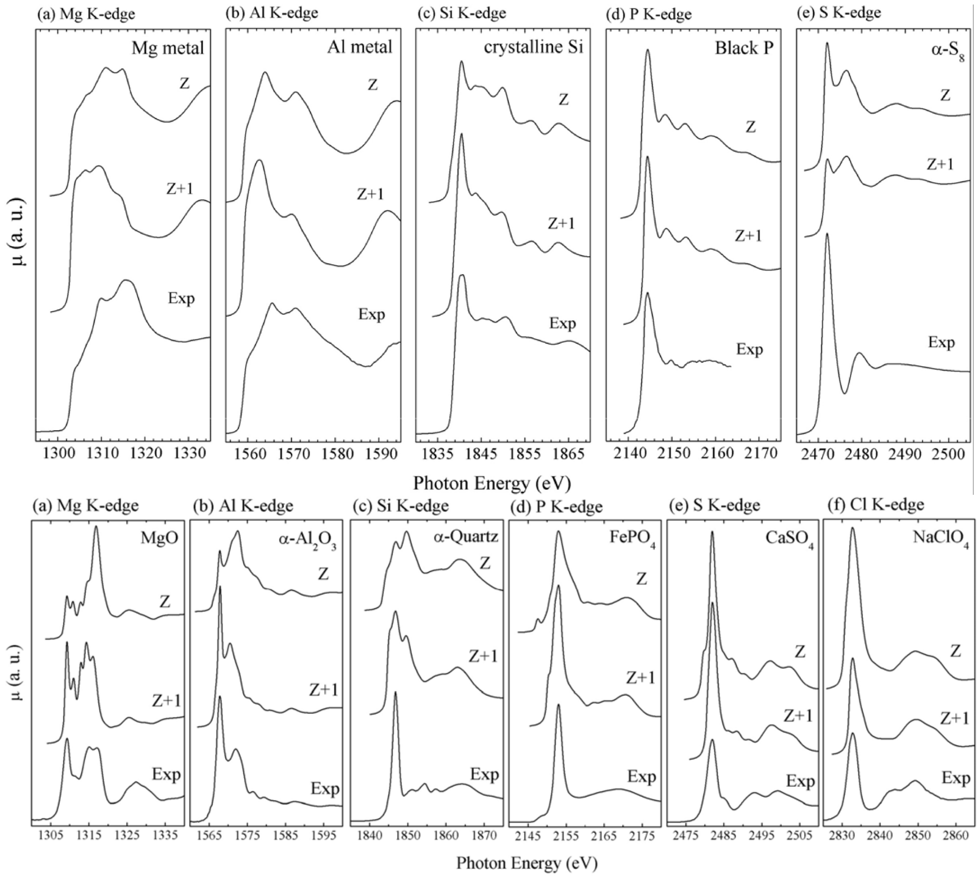

Figure 6.2: Experimental and calculated K-edge XANES spectra of third row elements and their some compounds reported by K Nakanishi *et al.*[3]. The calculations are performed by using FEFF with screened core hole and Z+1 approximation.

region and constant potential in interstitial region. The value of the potential constant is called ”Muffin-tin zero” and here we represent it $M_0$. The multiple scattering calculations are performed with varying $M_0$ in order to investigate the effect of the origin of the electrostatic potential.

## 6.3 Result and Discussion

Figure 6.3 (a) shows the results of screened core hole calculation for Si K-edge XANES spectra with varying the origin of the electrostatic potential. The calculated XANES spectra show anomaly rising at the absorption edge. The calculated result shows that the variation of $M_0$ tends to suppress the singular at the absorption edge. In order to investigate the reason why the absorption edge show the singularity, we check Si K-edge atomic absorption spectra of various $M_0$ shown in Fig. 6.3 (b). The atomic absorption term is described in (2.15) in §2.1. It is composed of Gaunt integral, which represents dipole selection rule and radial dipole integral, which describes the overlap between the core wave function and the photoelectron wave function at each photon energy. In this work, we focus on K-edge spectra. Therefore we only consider the case of $l = 1$.

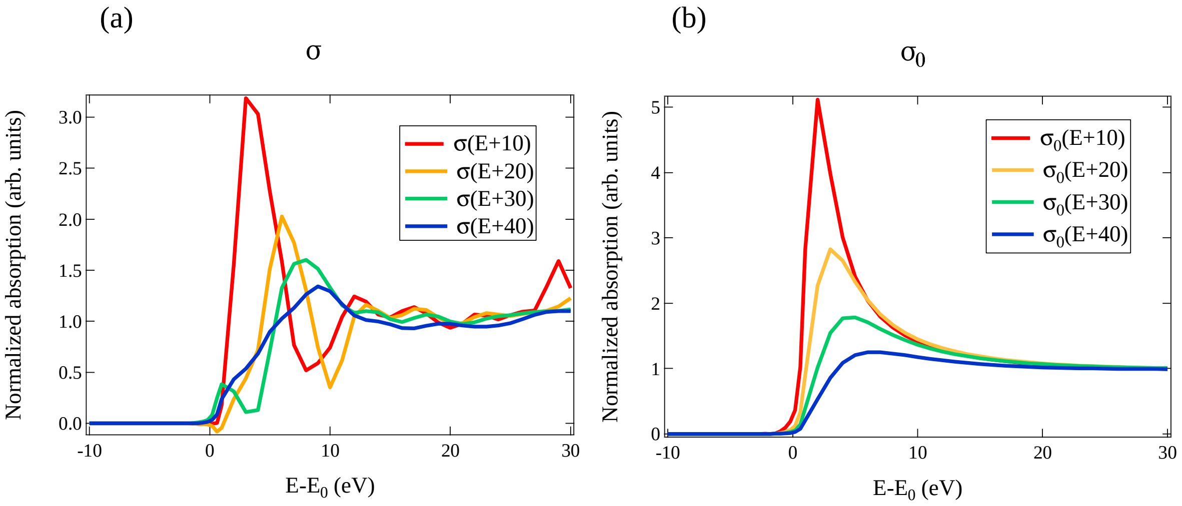

Figure 6.3: Calculated Si K-edge (a) XANES spectra (b) atomic absorption spectra with different values of $M_0$.

Figure 6.4 shows the radial dipole integral and the phase shift of $l = 1$. The radial dipole integral is described in (2.13) in §2.1. In the case of K-edge, the atomic absorption term is not affected by the phase shift and only depends on the radial dipole integral. The value of the radial dipole integral near the absorption edge is quite different between $M_0 + 10$ and $M_0 + 30$.

Figure 6.5 shows the overlap between Si 1$s$ core wave function and the photoelectron wave function of several photon energy. In the case of $M_0 + 10$, there is the large amount of overlap between Si 1$s$ and the photoelectron wave function with energy of 1 eV. On the other hand, in the case of $M_0 + 30$, the overlap between Si 1$s$ wave function and the photoelectron wave function with energy of 1 eV decreases compared with the case of $M_0 + 10$. Therefore the variation of $M_0$ reduces the overlap between core wave function and the photoelectron wave function.

Figure 6.6(a) shows the wave function of Si 1$s$ and 3$p$. The core function is

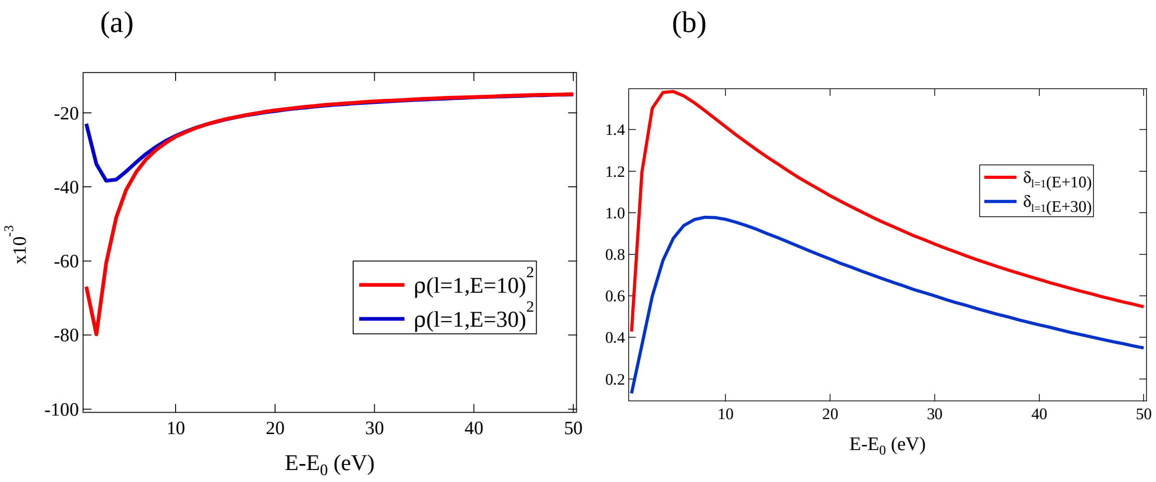

Figure 6.4: Calculated Si K-edge (a) radial dipole integral and (b) phase shift of $l$ = 1 with different $M_0$.

localized near the origin. However the valence orbital spreads beyond the muffin-tin radius $R_{mt}$. Therefore the charge inside the muffin-tin region is not neutral due to a small amount of charge outside of the region. Then it causes potential gap between muffin-tin region and interstitial region at muffin-tin radius. In the case of $M_0$ + 10, the gap is about 22 eV. This can be considered the reason why the resonance-like sharp shape at the absorption edge appears. On the other hand, the gap is about 4 eV for the case of $M_0$ + 30, and then the singularity reduces. From these results, the variation of $M_0$ reduces the potential gap and the value of radial dipole integral $\rho$. These effects make reduction of the singularity at the absorption edge.

Figure 6.7 shows the calculated results based on Z+1 approximation. The atomic absorption spectrum shown in Fig. 6.7(a) has the singular sharp at the absorption edge. The overlap between core function and the photoelectron wave function with photon energy 1 eV becomes large and then the radial dipole integral has a large amount. However, the gap of electrostatic potential at muffin-tin radius decreases. The value of the gap is about 5 eV.

Figure 6.8 shows the calculated results of P (Black) K-edge XANES and its atomic absorption spectra with various $M_0$. There are the sharp rising at the absorption edge and variation of $M_0$ reduces the singularity. These results have same tendency as the case of Si.

The radial dipole integral is shown in Fig. 6.9(a) and the overlap between the core wave function and the photoelectron wave function with $M_0 + 10$ and $M_0 + 30$ are shown in Fig. 6.9(c) and (d).

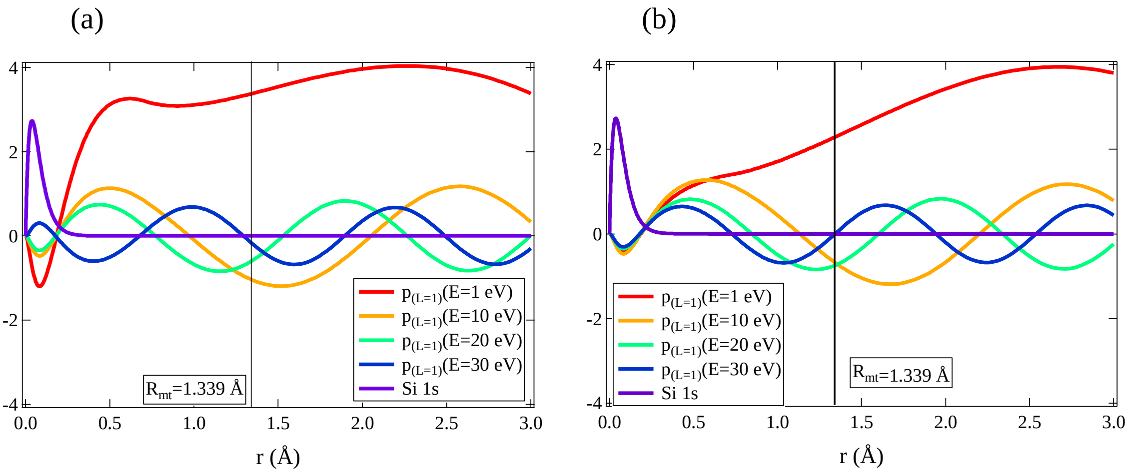

Figure 6.5: The core wave function of Si 1*s* and photoelectron wave function at various photoelectron energy for (a) $M_0$ + 10 and (b) $M_0$ + 30. The vertical line shows the muffin-tin radius.

Figure 6.10 shows the calculated results based on Z+1 approximation. The atomic absorption spectrum shown in Fig. 6.10(a) does not show the singularity. That is because the overlap decreases and then the radial dipole integral decreases. The gap of electrostatic potential is about 4.5 eV.

These calculations suggest that the variation of $M_0$ and Z+1 approximation makes the reduction of the potential gap.

Figure 6.11 shows the calculated Mg K-edge XANES and atomic absorption spectra with various $M_0$. The radial dipole integral, the gap of electrostatic potential, and the overlap between Mg 1*s* and the photoelectron wave function are shown in Fig. 6.12. Variation of $M_0$ reduces the singularity at the absorption edge. That is the same tendency as the case of Si and P.

In XANES analysis, Z+1 approximation is commonly used for light elements, but not for heavy elements. Figure 6.13(a) shows the calculated Ni K-edge XANES and its atomic absorption spectrum. The atomic absorption spectrum does not show the singularity at the absorption edge. The core function is localized near the origin, and then the overlap between Ni 1*s* core wave function and the photoelectron with energy of 1 eV is quite small. Therefore the value of the radial dipole integral becomes smaller. The gap of the electrostatic potential at the muffin-tin radius is also small, and its value is about 7 eV. Therefore the resonance-like singular shape at the absorption edge does not appear in the case of heavy element.

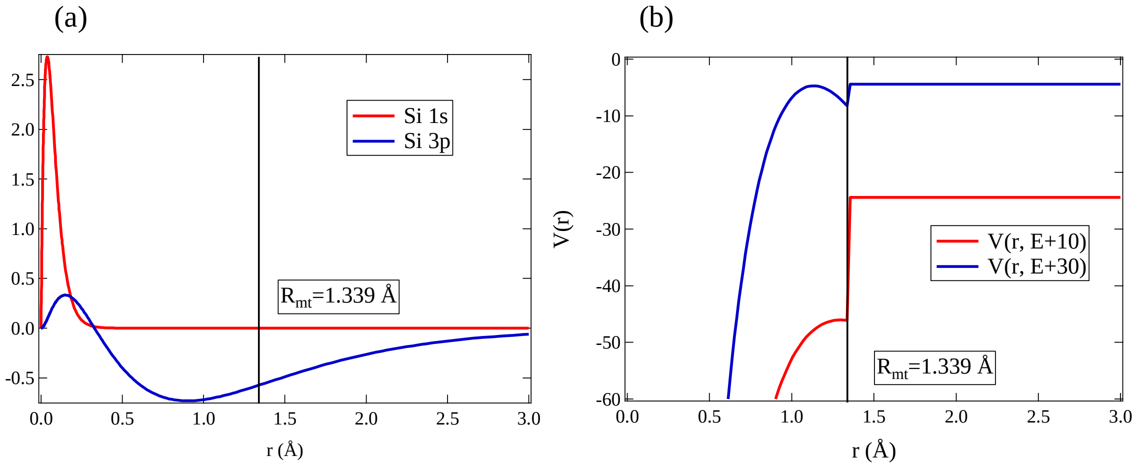

Figure 6.6: (a) The Si 1*s* and 3*p* wave function. (b) The electrostatic potential of X-ray absorbing Si for $M_0+10$ and $M_0+30$. The vertical lines show the muffin-tin radius.

## 6.4 Conclusion

In this section, we study K-edge XANES spectra of the third row elements. The calculated results show that the singularity appears at the absorption edge. This singularity is caused by large amount of the overlap between the core wave function and the photoelectron wave function with low energy and the gap of the electrostatic potential at the muffin-tin radius. The variation of $M_0$ reduces of the overlap and the potential gap. Therefore the singularity is suppressed. The Z+1 approximation also causes the reduction of the overlap and the gap of the electrostatic potential. Therefore the variation of $M_0$ and the Z+1 approximation affect to the XANES spectra. For heavy elements, K-edge XANES analysis is usually performed by using screened core hole calculation. The calculated result of Ni does not shows singularity at the absorption edge because the overlap between the core wave function and the photoelectron wave function and the gap of the electrostatic potential is quite small.

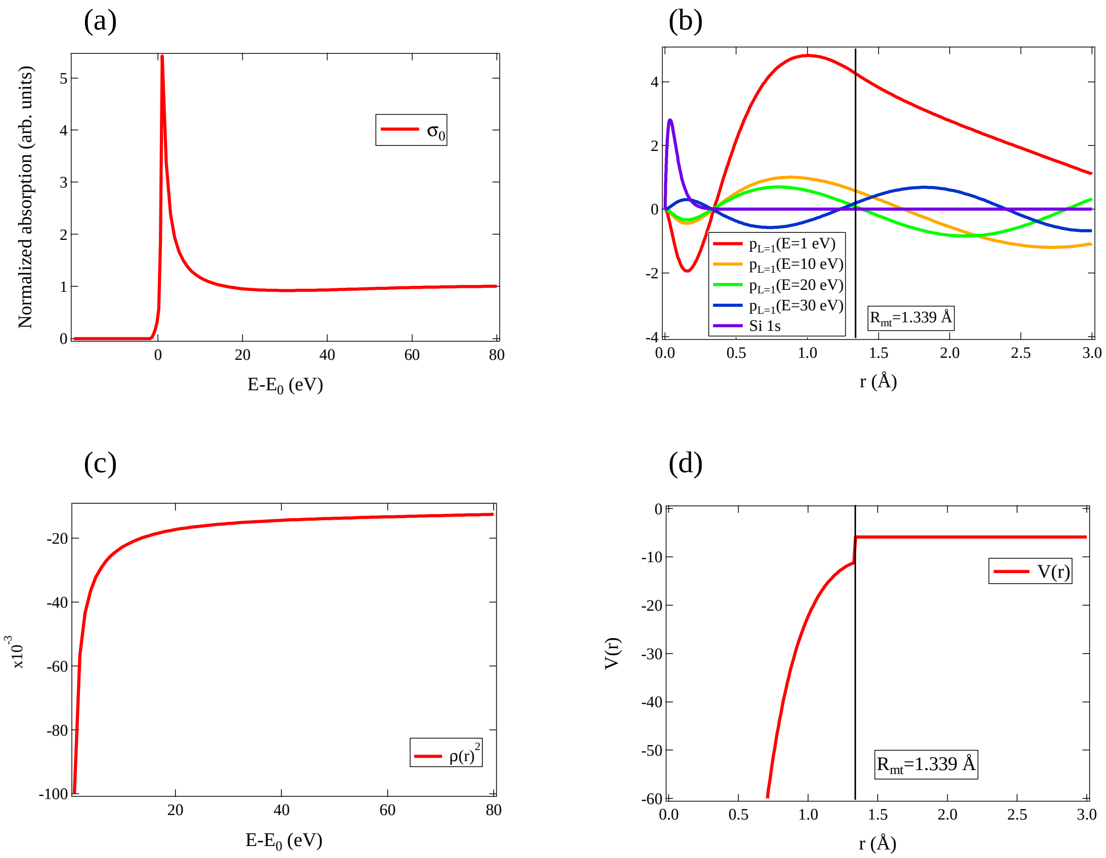

Figure 6.7: (a) The calculated Si K-edge atomic absorption spectrum (b) Si 1*s* core wave function and photoelectron wave function with several photon energy (c) radial dipole integral (d) electrostatic potential of X-ray absorbing Si. The vertical lines of (b) and (d) mean the muffin-tin radius. These calculations are performed using Z+1 approximation.

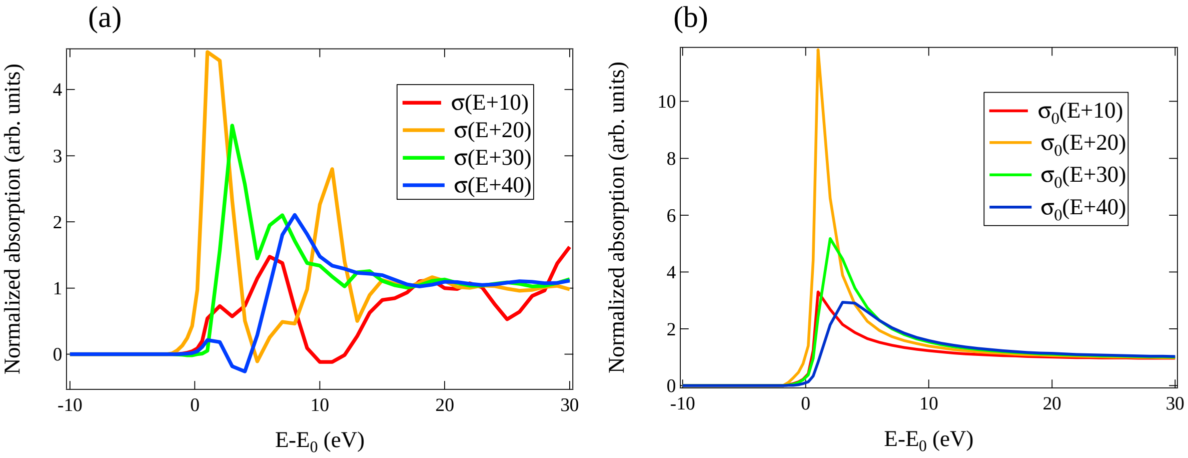

Figure 6.8: Calculated P K-edge (a) XANES spectra (b) atomic absorption spectra with different values of $M_0$.

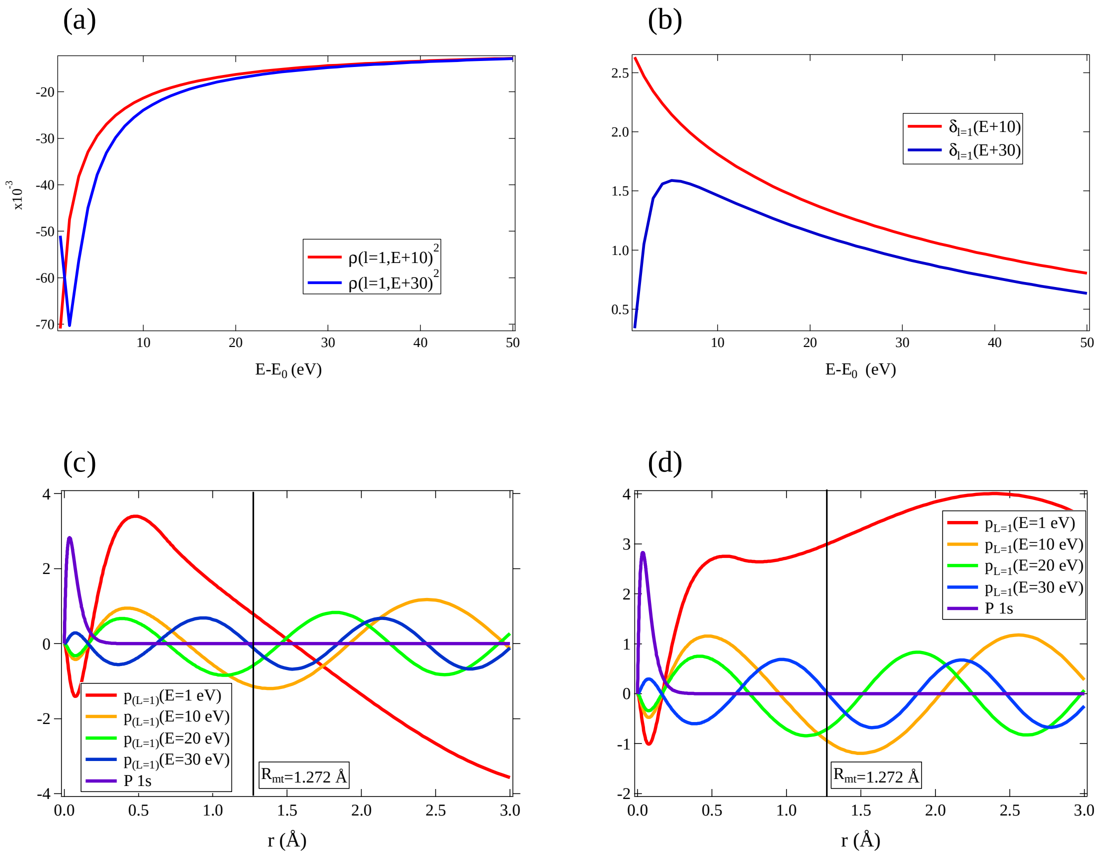

Figure 6.9: Calculated P (Black) K-edge (a) radial dipole integral and (b) phase shift of $l = 1$ (c) core wave function of P 1$s$ and photoelectron wave function with various energy of $M_0 + 10$ (d) core wave function of P 1$s$ and photoelectron wave function with various energy of $M_0 + 30$ The vertical line shows the muffin-tin radius.

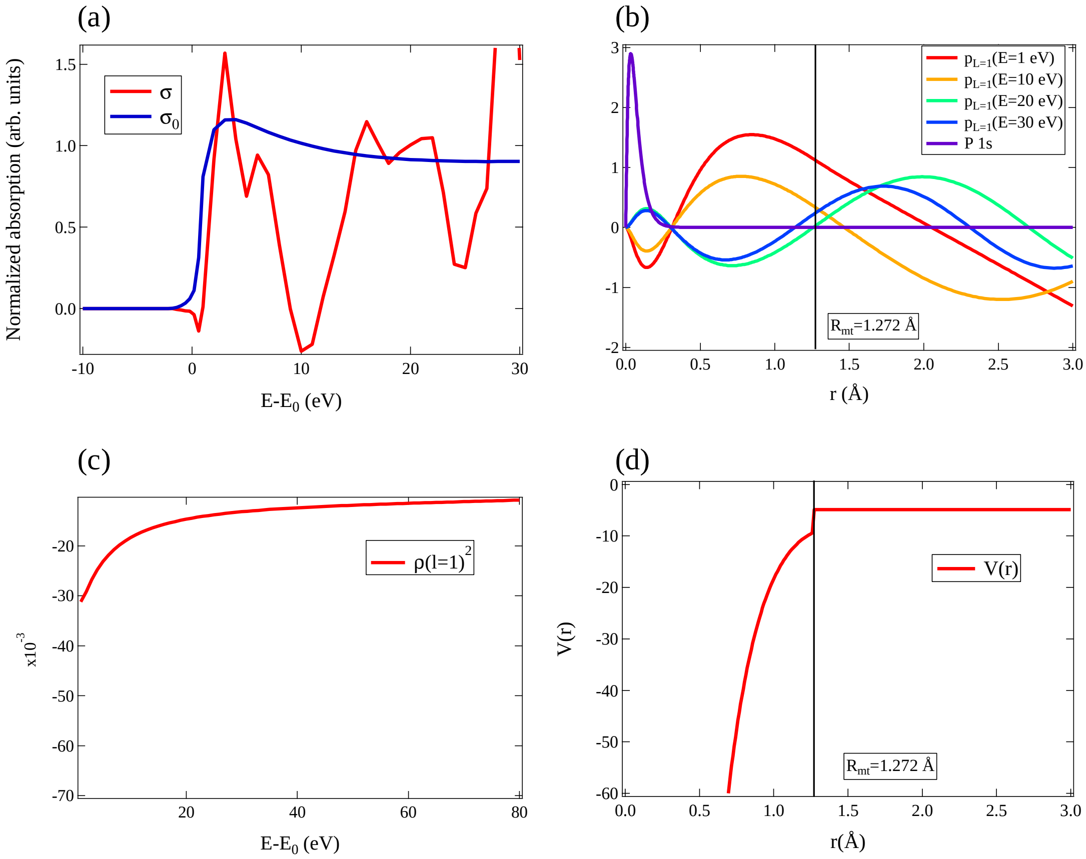

Figure 6.10: (a) The calculated P K-edge XANES and atomic absorption spectrum (b) P 1*s* core wave function and photoelectron wave function with several photon energy (c) radial dipole integral (d) electrostatic potential of X-ray absorbing P. The vertical lines of (b) and (d) mean the muffin-tin radius. These calculations are performed using Z+1 approximation.

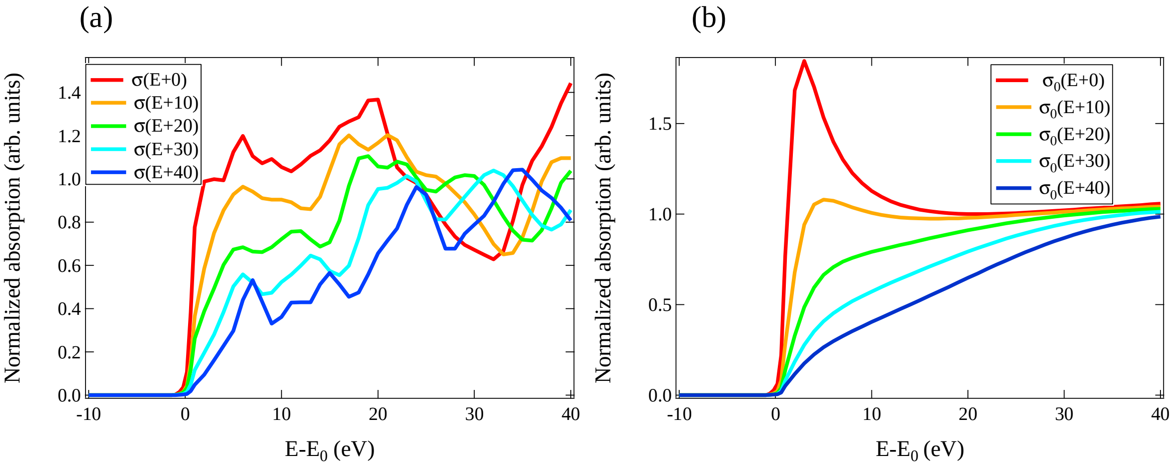

Figure 6.11: Calculated Mg K-edge (a) XANES spectra (b) atomic absorption spectra with different values of $M_0$.

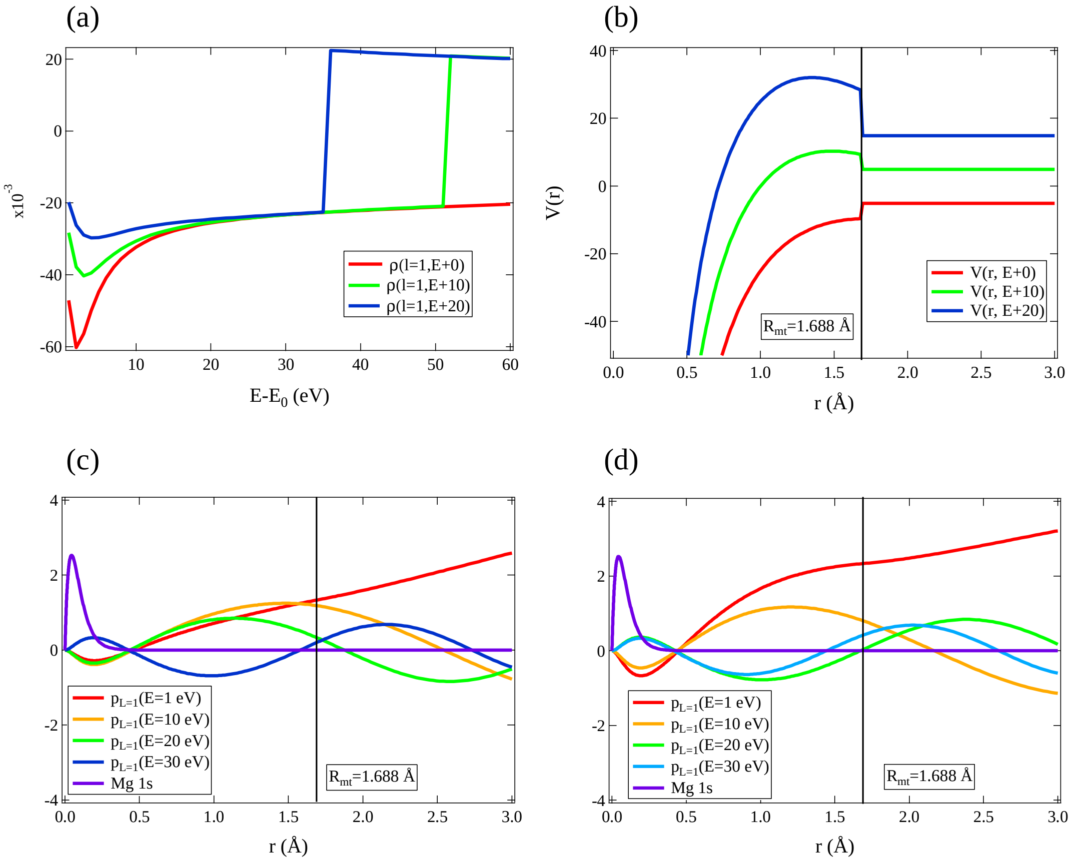

Figure 6.12: Calculated Mg K-edge (a) radial dipole integral of $l = 1$ (b) the electrostatic potential (c) core wave function of Mg 1$s$ and photoelectron wave function with various energy of $M_0 + 0$ (d) core wave function of Mg 1$s$ and photoelectron wave function with various energy of $M_0 + 20$ Vertical line shows the muffin-tin radius.

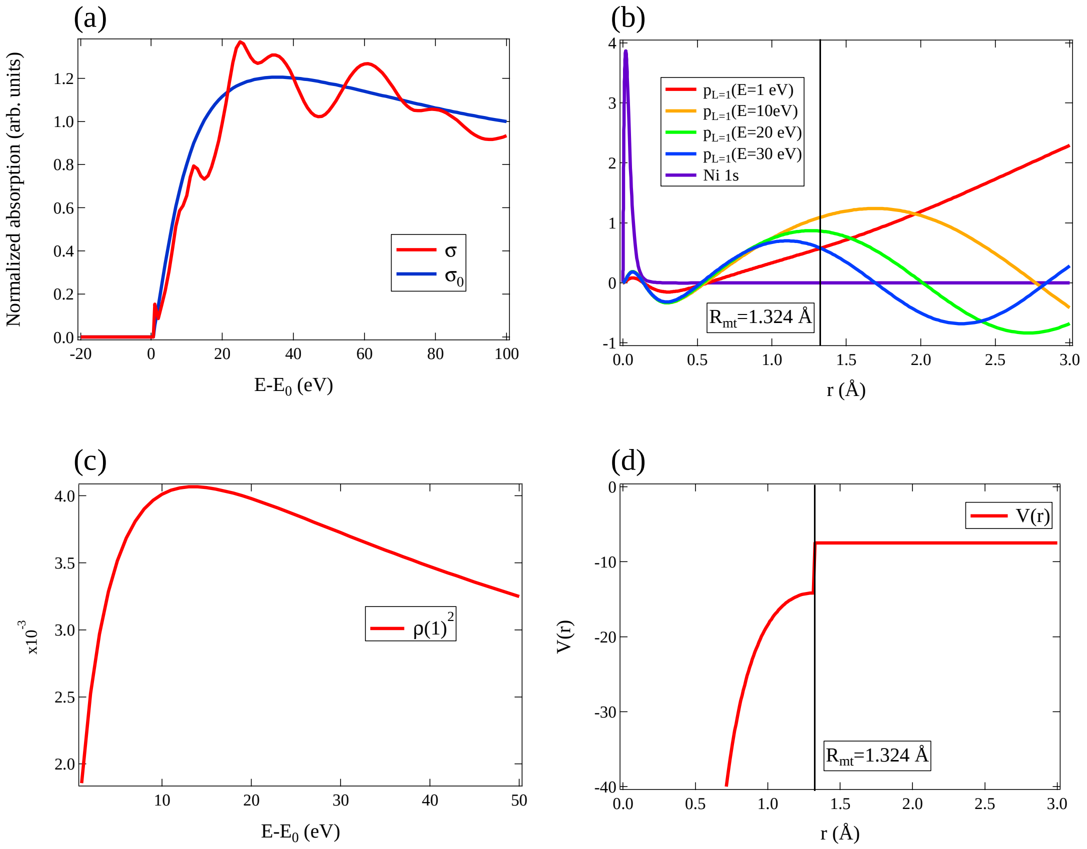

Figure 6.13: (a) The calculated Ni K-edge XANES and atomic absorption spectrum (b) Ni 1*s* core wave function and photoelectron wave function with several photon energy (c) radial dipole integral (d) electrostatic potential of X-ray absorbing Ni. The vertical lines of (b) and (d) mean the muffin-tin radius.

# Chapter 7

# Ni K-edge XAFS analysis of NiO thin film with multiple scattering theory

## 7.1 Introduction

X-ray absorption fine structure (XAFS) spectroscopy is one of the most useful techniques for determination of local structure around specific elements. One of the greatest benefit of XAFS spectroscopy is that we can apply this method to any types of the samples. Nickel oxide (NiO) thin films have wide range applications such as electrode material for supercapacitors [71], catalysts [72, 73, 74] and fuel cell system [75, 76] because of the specific properties. Non-stoichiometric nickel oxides are p-type semiconductors with wide band gaps ranging from 3 to 4 eV owing to the O defects [77]. A previous report found that the NiO thin film can also behave as n-type semiconductors when the samples are annealed above 200 °C. This behavior may be caused by the Ni defects [78]. The structural information around Ni in the NiO thin films is thus important to clarify the electron conduction mechanism, however, the conventional diffraction technique cannot be applied to them because of the low crystallinity. In this section, we report the Ni K-edge EXAFS and XANES analyses of the NiO thin films with different annealing temperatures.

## 7.2 Experimental

NiO thin films were deposited on the glass substrate with the deposition rate of 0.5 $\text{Å}/s$ by the electron-beam evaporation method under the pressure of $\sim 10^{-6}$ Torr. The base pressure was $10^{-8}$ Torr. During the deposition, the substrate holder was rotated at 5 rotations per minute (rpm). The physical thickness of the thin films was 50 nm. Thin films were post annealed at 100 °C and 300 °C for 30 minutes in vacuum. The X-ray absorption spectra (XAS) measurements were performed using transmission mode at Beam Line-8C in Pohang Light Source (PLS) in South Korea, and with the electron storage performance of 2.5 GeV and 200 mA. The fluorescence mode with 7-element Germanium solid-state detector (SSD) system was used in the XAS measurements and the data were collected and analyzed at the Ni K-edge near 8333 eV.

## 7.3 Result and Discussion

Figure 7.3 shows the comparison between the experimental and the calculated Fourier transformed Ni K-edge EXAFS spectra of NiO annealed at 100 °C and 300 °C. $k^2$ weighted spectra are Fourier transformed in the range of $k = 2 \sim 8$ Å$^{-1}$. The peak positions correspond to the distance between a Ni atom and its neighboring atoms. Note that the peak positions appear at shorter distance than the actual distance because of the scattering phase shifts. In this study, we discuss the peak position and the peak heights. There are five peaks (A-E peaks) which are ascribed to Ni-O (A), Ni-Ni (B), Ni-O (C), Ni-Ni, Ni-Ni-O, Ni-O-Ni-O, Ni-O (D) and Ni-Ni (E) scattering paths, respectively. In order to analyze the EXAFS, we consider the spherical cluster models with radius of 8 Å [69, 79]. The space group is $Fm\bar{3}m$ and the cubic lattice parameter $a = 4.1684$ Å for NiO crystal. The calculated spectra are obtained by use of FEFF8 code and Fourier transformed by Artemis [80, 60]. The calculated intensities for the peaks C-E are overestimated because the structural model is based on the crystal structure which neglect the disorder. For the sample annealed at 100 °C, the peaks A and B are slightly shifted to a shorter distance than those annealed at 300 °C. For the sample annealed at 300 °C we use the structural parameters for NiO crystal the nearest distances of Ni-O and Ni-Ni are 2.084 Å and 2.947 Å but two Ni atoms in the second shell are excluded. The calculated result and the experimental EXAFS spectrum are good agreement for the peaks A and B as shown in Fig. 7.3. On the other hand for the sample annealed at 100 °C we keep the NiO structure but only change the Ni-O distance. We have obtained the best result from the slightly shortened structure whose distance between Ni and O from the crystal structure where $d(Ni-O) = 1.984$ Å and $d(Ni-Ni) = 2.747$ Å. The calculated result is not so good at 100 °C compared with that at 300 °C, since the static disorders should make the fit difficult. In the case of the sample annealed at 100 °C, the ratio of the height of peak A to that of peak B is 0.762 in the experimental spectrum and 0.688 in the calculated spectrum. On the other hand, at annealing temperature of 300 °C, the ratio is 0.839 in the experimental spectrum, and 0.834 in the calculated

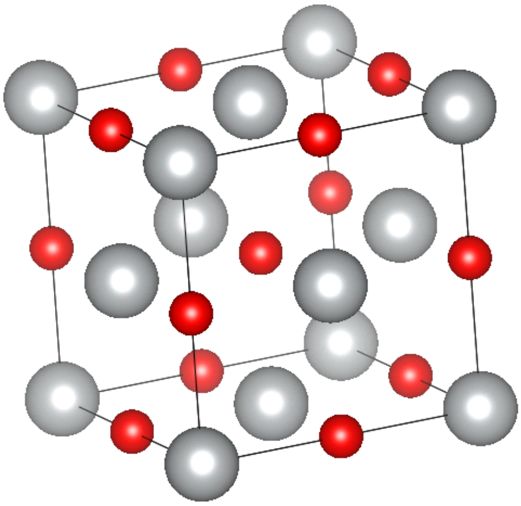

Figure 7.1: NiO unit cell structure. Silver circles mean Ni and red circles mean O atoms.

spectrum. For the sample annealed at 300 °C, the ratio is well explained by the calculated result. It clarifies the NiO thin film annealed at 300 °C has defects of Ni. It is consistent with the results of NiO thin film which behave as *n*-type semiconductor above annealing temperature of 200 °C. For that at 100 °C, the calculated ratio does not coincide with the experimental ratio. The disagreement of the ratio between the experimental and the calculated results suggests that there are some amounts of the O defects. Although the peak E is contributed by a single scattering path from fourth Ni shell, the peak has a large magnitude due to the focusing effect which is caused by the linearly arrangement of the atoms. This peak may be useful to estimate the crystallinity of the film. Thus, the local structure around Ni in the sample annealed at 300 °C may be resemble to its crystal structure.

Table 7.1: Calculation model information

| | 100 °C | 300 °C |
|---|---|---|
| Distance of Ni-O (Å) | 1.984 | 2.084 |
| Distance of Ni-Ni (Å) | 2.747 | 2.747 |
| Coordination number of O | 6 | 6 |
| Coordination number of Ni | 12 | 10 |

Figure 7.4 shows the experimental and the calculated Ni K-edge XANES spectra of the samples annealed at 100 °C and 300 °C. The experimental Ni K-edge

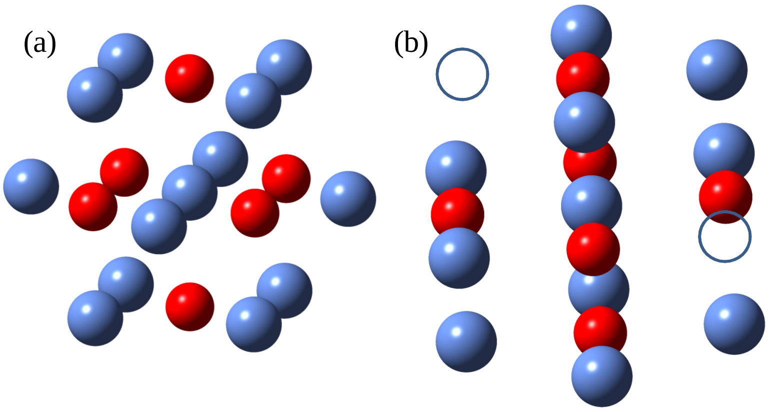

Figure 7.2: Calculation models up to second shell for the sample annealed at (a) 100 °C and (b) 300 °C. In the case of (b), two Ni atoms in second shell are excluded (blue circle).

XANES spectra are quite different for different annealing temperature. The disordered systems typically show structureless XANES spectra. The observed result indicates prominent disorder in the sample annealed at 100 °C. If we can fit the peaks A and B, we may estimate the disorder of the samples. The pre-edge peaks are observed around 8335 eV at the both annealing temperature. Usually, the pre-edge peak is not only due to the quadrupole transition but also due to the dipole transition because of d-p hybridization [81]. For the sample annealed at 300 °C, the pre-edge peak is considered to be the direct dipole transition Ni 1$s$ → O 2$p$ due to the strong hybridization [82]. The models are constructed from the crystal structure [69] in order to perform multiple scattering calculations. The cluster radii are 8 Å with 251 atoms for the model annealed at 100 °C, and 249 atoms for the model of the sample annealed at 300 °C. In the structural model for the sample annealed at 100 °C, the distances to the nearest O atoms and Ni atoms are shortened 0.1 Å and 0.2 Å from the case of NiO crystal refereeing to the EXAFS result. In the structural model for the sample annealed at 300 °C, two Ni atom in the second shell are excluded. The calculated XANES spectra well agree with the experimental spectra. This implies the reliability of the models used in this study.

From the EXAFS and XANES analyses, the local structures around Ni of the NiO thin films are explained by the model structures constructed from the crystal. The crystallinity of the NiO thin film depends on the annealing temperature.

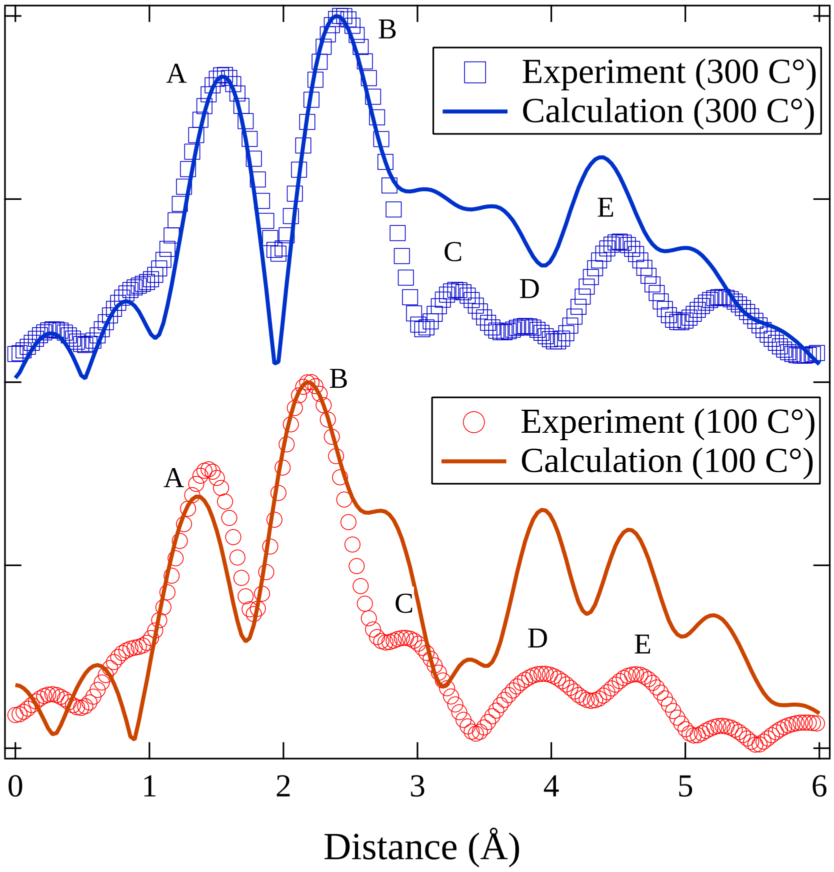

Figure 7.3: Experimental and calculated Ni K-edge Fourier transformed EXAFS spectra of the sample annealed at 100 °C and 300 °C.

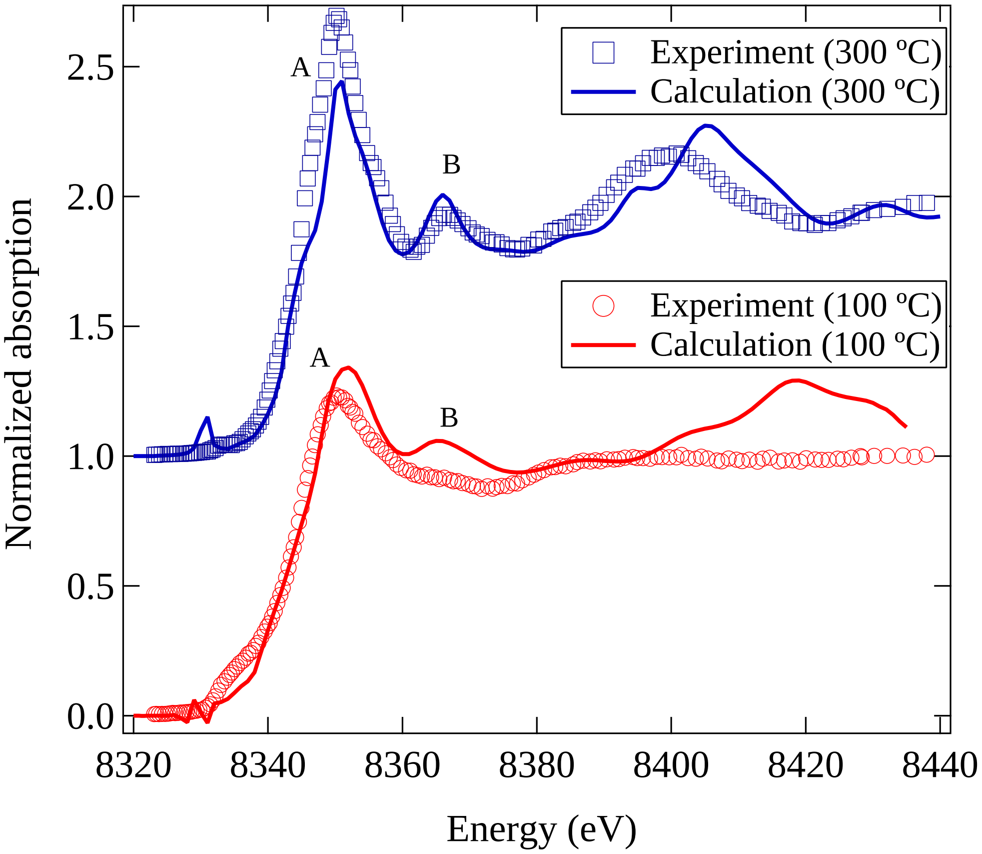

Figure 7.4: Experimental and calculated Ni K-edge XANES spectra of the sample annealed at 100 °C and 300 °C.

## 7.4 Conclusion

We study the Ni K-edge XAFS spectra of NiO thin films annealed at 100 °C and 300 °C. The EXAFS and the XANES spectra show that the crystallinity depends on the annealing temperature. The high annealing temperature produces the high crystallinity of the NiO thin films. In the experimental Fourier transformed EXAFS spectra, the Ni-O and Ni-Ni peaks are slightly shifted to shorter distance. In the NiO thin film sample annealed at 100 °C, the distances between Ni-O and Ni-Ni are 1.984 Å and 2.747 Å, respectively. In the sample annealed at 300 °C, the distances between Ni-O and Ni-Ni are 2.084 Å and 2.947 Å. The ratios of the peak height of Ni-O to Ni-Ni are 0.762 in the sample annealed at 100 °C, and 0.839 in the sample annealed at 300 °C. The calculated ratios are 0.688 in the model of the samples annealed at 100 °C and 0.834 in the model of the samples annealed at 300 °C which suggest some amount of defects. The experimental Ni K-edge XANES spectra are well explained by use of multiple scattering calculations.

# Bibliography

[1] W. H. McMaster, N. K. D. Grande, J. H. Mallett, and J. H. Hubbell, *Compilation of X-ray Cross Sections*, Lawrence Livermore National Laboratory Report, 1969.

[2] M. Sommerhalter, Y. Zhang, and A. C. Rosenzweig, J. Mol. Biol. **365**, 715 (2007).

[3] K. Nakanishi and T. Ohta, J. Phys.: Condens. Matter (2009).

[4] R. D. Kronig, Z. Phys **75**, 468 (1932).

[5] D. E. Sayers, E. A. Stern, and F. W. Lytle, Phys. Rev. Lett. **27**, 1204 (1971).

[6] *Fundamentals of XAFS*, `http://xafs.org/Tutorials?action=AttachFile&do=get&target=Newville_xas_fundamentals.pdf`, 2008.

[7] *X-Ray Absorption: PRINCIPLES, APPLICATIONS, TECHNIQUES OF EXAFS, SEXAFS AND XANES*, JOHN WILEY & SONS, 1988.

[8] `http://133.50.165.193/catdb/`.

[9] T. Ishii, editor, *Basic of EXAFS*, Shokabo, 3 edition, 1994.

[10] e. T. Ohta, editor, *X-ray absorption spectroscopy:XAFS and the application*, IPC Inc., 3 edition, 2002.

[11] T. McKee and J. R. McKee, editors, *BIOCHEMISTRY The Molecular Basis of Life*, Kagaku Doujin, 3 edition, 2005.

[12] A. K. Katz et al., Helvetica Chimica Acta **86**, 1320 (2003).

[13] A. Ala, A. P. Walker, K. Ashkan, J. S. Dooley, and M. L. Schilsky, THE LANCET **369**, 397 (2007).

[14] A. I. Bush, Curr. Opin. in Chem. Biol. **184**, 184 (2000).

[15] P. de Bie, B. van de Sluis, L. Klomp, and C. Wijmenga, The Journal of Heredity **96**, 803 (2005).

[16] E. Burstein et al., J. Biol. Chem. **280**, 22222 (2005).

[17] S. Narindrasorasak, P. Kulkarni, P. Deschamps, Y.-M. She, and B. Sarkar, Biochemistry **46**, 3116 (2007).

[18] N. Yonezawa, (in preparation).

[19] P. de Bie et al., Biochem. J. **398**, 63 (2006).

[20] M. Nomura, KEK report **98-4** (1998).

[21] T. Akai, M. Okuda, and M. Nomura, Bull. Chem. Soc. Jpn. **72**, 1239 (1999).

[22] T. Hasegawa and Y. Ozaki, BUNSEKI KAGAKU [in Japanese] **54**, 1 (2005).

[23] E. R. Malinowski, editor, *Factor Analysis in Chemistry*, Wiley-Interscience, 3 edition, 2002.

[24] A. Mishra, N. Parsai, N. Soni, and B. D. Shrivastava, J. Phys.:Conf. Ser. **365**, 012016 (2012).

[25] L.-S. Kau, D. J. Spira-Solomon, J. E. Penner-Hahn, K. O. Hodgson, and E. I. Solomon, J. Am. Chem. Soc. **109**, 6433 (1987).

[26] M. J. Frisch et al., Gaussian 09 Revision B.01, 2009, Gaussian Inc. Wallingford CT 2009.

[27] M. Pavelka, M. Šimánek, J. Šponer, and J. V. Burda, J. Phys. Chem. A **110**, 4795 (2006).

[28] N. Kosugi, T. Yokoyama, K. Asakura, and H. Kuroda, Chemical Physics **91**, 249 (1984).

[29] J. Chaboy, A. M. noz Páez, F. Carrera, P. Merkling, and E. S. Marcos, Phys. Rev. B **71**, 134208 (2005).

[30] A. L. Ankudinov, A. I. Nesvizhskii, and J. J. Rehr, Phys. Rev. B **67**, 115120 (2003).

[31] J. J. Rehr and R. C. Albers, Rev. Mod. Phys. **72**, 621 (2000).

[32] I. Presson, Pure Appl. Chem. **82**, 1901 (2010).

[33] V. S. Bryantsev, M. S. Diallo, A. C. T. van Duin, and W. A. G. III, J. Phys. Chem. **112**, 9104 (2008).

[34] A. I. Frenkel, G. V. Korshin, and A. L. Ankudinov, Environ. Sci. Technol. **34**, 2138 (2000).

[35] H. Ohtaki and M. Maeda, Bull. Chem. Soc. Jpn. **47**, 2197 (1974).

[36] *Phthalocyanine Materials - Synthesis, Structure and Function*, Cambridge University Press, 1998.

[37] T. Inabe and H. Tajima, Chem. Rev. (2004).

[38] *Phthalocyanines:Properties and Applications*, Wiley, 1986-1993.

[39] S. Rajaputra, S. Vallurupalli, and V. P. Singh, J. Mater. Sci.: Mater. Electron (2007).

[40] M. Garcia-Iglesias et al., Energy Environ. Sci. (2011).

[41] M. L. Rodriguez-Mendez and J. A. de Saja, J. Porphyrins Phthalocyanines (2009).

[42] N. Hanasaki, H. Tajima, M. Matsuda, T. Naito, and T. Inabe, Phys. Rev. B **62**, 5839 (2000).

[43] N. Hanasaki et al., J. Phys. Soc. Jpn. **75**, 033703 (2006).

[44] M. Matsuda et al., J. Mater. Chem. **10**, 631 (2000).

[45] D. E. C. Yu et al., J. Matter. Chem. **19**, 718 (2009).

[46] C. Hotta, M. Ogata, and H. Fukuyama, PRL (2005).

[47] C. Hotta, Phys. Rev. B (2010).

[48] M. Benfatto, J. A. Solera, J. G. Ruiz, and J. Chaboy, Chem. Phys. (2002).

[49] I. Arčon, J. Kolar, A. Kodre, D. Hanžel, and M. Strlič, X-Ray Spectom. (2007).

[50] F. de Groot, G. Vankó, and P. Glatzel, J. Phys.:Condens. Matter (2009).

[51] D. Cabaret, A. Bordage, A. Juhin, M. Arfaoui, and E. Gaudry, Phys. Chem. Chem. Phys. (2010).

[52] F. Frarges, Phys. Rev. B (2005).

[53] *Polyvinyl alcohol fibers.*, Wiley New York, 1985.

[54] Y. Oishid and K. Miyasaka, Polym. J. (1986).

[55] Y. Choi, Y. Oishi, and K. Miyasaka, Polym. J. (1990).

[56] Y. Choi and K. Miyasaka, J. Appl. Polym. Sci. (1993).

[57] H. Takamiya et al., J. Appl. Polym. Sci. (1993).

[58] T. Yokoyama, K. Kaneyuki, H. Sato, H. Hamamatsu, and T. Ohta, Bull. Chem. Soc. Jpn. (1995).

[59] T. Miki et al., J. Phys. Conference (2009).

[60] B. Ravel and M. Newville, J. Synchrotron Rad. (2005).

[61] H. Sakane, T. Mitui, H. Tanida, and I. Watanabe, J. Synchrotron Rad. (2001).

[62] H. Ebert, D. Ködderitzsch, and J. Min*á*r, Rep. Prog. Phys. (2011).

[63] O. Peyrusse, J. Phys.: Condens. Matter (2008).

[64] Z. Wu et al., Phys. Rev. B (1999).

[65] J. A. van Bokhoven, T. Nabi, H. Sambe, D. E. Ramaker, and D. C. Koningsberger, J. Phys.: Condens. Matter (2001).

[66] E. Tanuma, J. van Ek, M. Fröba, and J. Wong, Phys. Rev. Lett. (1995).

[67] D. Cabaret, P. Sainctavit, P. Ildefonse, and A.-M. Flank, J. Phys.: Condens. Matter (1996).

[68] D. Cabaret and C. Brouder, J. Phys.: Conf. Ser. (2009).

[69] `http://cars9.uchicago.edu/~newville/adb/search.html`.

[70] `http://mits.nims.go.jp/`.

[71] K. Lota, A. Sierczynska, and G. Lota, International Journal of Electrochemistry (2011).

[72] J. C. N. Botejue and A. C. C. Tseung, J. Electrochem. Soc. (1985).

[73] K. M. Dooly, S. Y. Chen, and J. R. H. Ross, J. Catal. (1994).

[74] A. Alejandre, F. Medina, P. Salagre, A. Fabregat, and J. E. Sueiras, Appl. Catal. B (1998).

[75] F. Li, H. Chen, C. Wang, and K. Hu, J. Electroanal. Chem. (2002).

[76] Y. Hattori, T. Konishi, and K. Kaneko, Chem. Phys. Lett. (2002).

[77] R. Palombari, J. Electroanal. Chem. (2003).

[78] P. Gupta, T. Dutta, S. Mal, and J. Narayan, Journal of Applied Physics (2012).

[79] S. P. Srivastava, R. C. Srivastava, I. D. Singh, S. D. Pandey, and P. L. Gupta, J. Phys. Soc. Jpn. (1977).

[80] J. J. Rehr, J. M. de Leon, S. I. Zabinsky, and R. C. Albers, J. Am. Chem. Soc. (1991).

[81] Y. Yamamoto, X-Ray Spectrum. (2008).

[82] C. Gougoussis et al., Phys. Rev. B (2009).